Universiteit Utrecht

Opleiding Natuur- en Sterrenkunde

Asymptotic Analysis of non-Linear Sand Transport in Estuaries

Bachelor Thesis

Jelle Soons

Supervisors
Prof. Dr. H.E. de Swart
University Utrecht
T.M. Hepkema, Msc.
University Utrecht

June 12th, 2019

Abstract

Asymptotic analysis is applied to a two-dimensional depth-averaged morphodynamic model for a tidally dominated estuary. The water motion is described by the depth-averaged shallow water equations and driven by an externally prescribed M_2-tide. The sediment transport is determined by the tidal averages of suspended sediment and sediment as bed load transport. The linearized equations can quantitatively denote the tidal bar length, and can be used qualitatively to clarify the physical processes behind the instability of the sandy bed. The second- and third-order equations are used to capture the non-linear morphodynamics of the estuary. The elongation of troughs and the shallow cross-channel sandy bridges of sand are reproduced. A finite-amplitude equilibrium could not be found.

Contents

1 Introduction

The topography of the sandy bottom of many shallow, tidally dominated estuaries are characterized by the presence of periodic patterns, consisting of so-called tidal bars. Some main examples are the Exe estuary in England, the Netarts bay in USA and the Western Scheldt in the Netherlands, see figures 1, 2 and 3. These bars have wavelengths of 1-15 km and have an height of several meters above the main average bottom. Since tidal bars are rich feeding grounds for birds, play valuable roles in marine life ecosystems, and can hamper marine traffic, it is important to understand the relations between main estuary characteristics, like channel width and average depth, and the resulting bottom topography, like tidal bar wavelength and amplitude. Furthermore, they are also an interesting scientific phenomenon, as they are the result of the complex interactions between the water motion and the sandy network of shoals and channels.

1.1 Overview of some past research

Some empirical studies of estuaries have been done. One in particular is Leuven et al.(2016)[9]. They measured (parts of) 190 estuaries using Google Earth and found some interesting correlations. Especially the correlation between channel width and tidal bar length is profound: a wider channel is correlated with longer tidal bars.
There have also been extensive numerical simulations. For example Jeuken (2000)[7] simulated the Western Scheldt using a process based model. The resulting water motion and sediment transport corresponded quite well with the observations. However, due to the complex structure of the numerical program it is difficult to extract any basic physical understanding about the causing processes. Therefore more simplified models are needed.
These simplified models have highly schematized geometries and are based on only a few equations for water motion and sediment transport. Their relative simplicity allows them to be analyzed using standard mathematical techniques, like Fourier analysis. This way it is possible to formulate basic theoretical relationships of these tidally dominated estuaries.
Using a simple three-dimensional model for narrow and frictionally dominated channels, Seminara & Tubino (2001)[14] showed that due to inherent instability of a flat sandy bottom these tidal bars can be formed. Schramkowski et al (2002)[12] extended the model to be applicable to wider basins that are not necessarily frictionally dominated and proved that three-dimensional effects and quadratic bottom stress are not necessary for the formation of these tidal bars: a two-dimensional model with depth-averaged shallow water equations and linearized bottom stress is sufficient. This simplified model also allowed for an extensive description of the physical processes behind this instability. Van der Wegen et al. (2008)[16] even used a one-dimensional model, but concluded the two-dimensional model to give the best estimate. Next, Schramkowski et al (2004)[13] showed that stable equilibria in the channel are possible for near-critical conditions when incorporating non-linear dynamics. Finally, Hepkema et al. (2019)[5] found, however, that linear mechanics alone are sufficient to explain the important relationship between channel width and tidal bar length by also incorporating horizontal eddy diffusivity.

1.2 Research question

Van Veelen et al. (2018)[17] analyzed large scale bed forms in shallow shelf seas. They used asymptotic analysis, where a truncated expansion of the important variables is made, in order to analyze the non-linear dynamics at different orders of magnitude. That way, it is possible to get a basic understanding of the most simple cases of the non-linear processes, without relying on complex numerical computations.
Combining the method of Van Veelen et al. (2018) with the current models of tidally dominated estuaries

is the main goal of this thesis. Important to remember is that Van Veelen looked at shallow shelf seas with open boundaries, whereas the estuary-models are bounded in the cross-channel direction. This leads to the main research question: can the same methods of asymptotic analysis be applied to the two-dimensional model of the tidally dominated estuary? More specifically, what parts of the non-linear dynamics, seen by Schramkowski et al. (2004) can be reproduced using second and third order asymptotic expansion? Would it for example be possible to create an equilibrium with second and third order dynamics? If this is indeed the case, then this would be a relatively simple analytical model to explain some important non-linear characteristics of estuaries.
Hence the main goal is to apply asymptotic analysis to a simplified model of a tidally dominated estuary with the intend to recreate the non-linear effects observed in Schramkowski et al.(2004). This way, asymptotic analysis may give a basic understanding of these non-linear dynamics.

Figure 1: The Western Scheldt, an exceptionally wide estuary in the Netherlands, figure from *Google Earth*. Note that some form of periodicity can be observed in the tidal bars.

Figure 2: The Netars Bay, a common estuary on the west coast of the USA, figure from *Google Earth*. A similar pattern can be observed here.

Figure 3: The Exe estuary, a common estuary on the south coast of England, figure from *Google Earth*. Also here a periodicity in the bathymetric patterns can be seen.

2 Model

The model is based on the model used in Hepkema et al(2018). It is a two-dimensional model: hydrodynamics and sediment transport are described with depth-averaged variables on a two-dimensional plane with coordinates $\vec{x} = (x, y)$[m].

2.1 Model description

Observations show that the bathymetric features in tidally dominated estuaries are relatively short compared to the tidal length of the estuary. Furthermore, it is assumed that the effects of channel width variations on the behaviour of these features are negligible. Therefore, the model of the estuary is represented as an infinitely long channel with constant width B[m]. Then a section with length L[m] is taken, with open boundaries at the end, to represent the whole channel. How length L will be determined, will be discussed later. Also, the banks are taken to be straight and non-erodible walls. The only feature subjected to erosion is the sandy bed itself.
The free surface level is denoted by ζ with undisturbed water depth $D = H - h$, where H[m] is a reference depth and h[m] the bed elevation with respect to the reference level $z = -H$. The along-channel and cross-channel currents are u, v[ms^{-1}] respectively, with $\vec{u} = (u, v)$. We use Cartesian coordinates $\vec{x} = (x, y)$ for along-channel and cross-channel directions, while z[m] is height, with $z = 0$ reference surface height. Finally, time is denoted by t. The model is depicted in figure 4 .

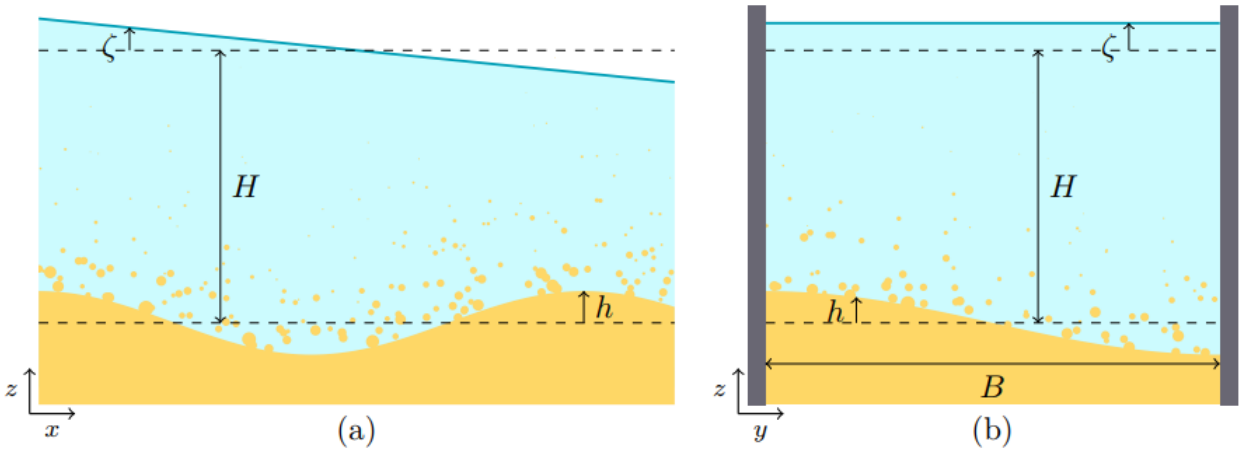

Figure 4: (a) The along-channel section in the (x, z)-plane. (b) The cross-channel-section in the (y, z)-plane.
H denotes the undisturbed depth, ζ the free-surface elevation, h the bed height and B the channel width. The arrows with x, y and z denote the direction of the spatial coordinates.
Source: Hepkema et al. (2019) [5].

2.2 Model equations

2.2.1 Depth-averaged shallow water equations

The tidal hydrodynamics are governed by the depth-averaged shallow water equations, where the rigid lid approximation is used. In the rigid-lid approximation all free surface gradients are neglected, except for those in the pressure gradient force. Furthermore, Coriolis effects are neglected and linearized bottom

stresses are used.
The continuity equation, based on mass conservation, is as follows:

$$\frac{\partial}{\partial x}((H-h+\zeta)u)+\frac{\partial}{\partial y}((H-h+\zeta)v)=0,$$

which is equivalent to volume conservation, since incompressibility is assumed. Then under the rigid-lid approximation the free surface gradients drop out, to yield:

$$\frac{\partial}{\partial x}((H-h)u)+\frac{\partial}{\partial y}((H-h)v)=0.$$

This can be rewritten to the following form:

$$(H-h)(\frac{\partial u}{\partial x}+\frac{\partial v}{\partial y})=u\frac{\partial h}{\partial x}+v\frac{\partial h}{\partial y}$$

The depth-averaged shallow water equations for along-channel and cross-channel current velocities are respectively:

$$\frac{\partial u}{\partial t}+(\vec{u}\cdot\nabla)u+\frac{ru}{H-h}-\nu\nabla^2u=(\vec{F}_p)_x$$
$$\frac{\partial v}{\partial t}+(\vec{u}\cdot\nabla)v+\frac{rv}{H-h}-\nu\nabla^2v=(\vec{F}_p)_y.$$

In these equations $\vec{F}_p=-g\nabla\zeta$ is the pressure-gradient force per unit mass, with $g[\mathrm{ms}^{-2}]$ the gravitational acceleration and $\zeta(\vec{x},t)[\mathrm{m}]$ the free surface elevation as stated earlier. Note that $\nabla=\left(\frac{\partial}{\partial x},\frac{\partial}{\partial y}\right)$ in this two-dimensional model. Furthermore, $\nu\nabla^2\vec{u}$ is a dissipation term to eddy viscosity, with $\nu[\mathrm{m}^2\mathrm{s}^{-1}]$ the horizontal eddy viscosity coefficient. As friction force $\vec{F}_r=\frac{r\vec{u}}{H-h}$ is used, inversely proportionate to depth D, the water depth, and with friction coefficient $r[\mathrm{ms}^{-1}]$. This is a linear parameterization for the friction force as first proposed by Lorentz (1922)[10]. In Schramkowski et al.(2002) it is shown that the same overall results are obtained using either linear or quadratic friction forces. A derivation of the depth-averaged shallow water equations can be found in Hepkema (2016) [4]. A more explicit interpretation on the rigid-lid approximation can be found in "Geophysical Fluid Dynamics" [2].

2.2.2 Vorticity equations

Based on Van Veelen et al. (2018) the equations for current velocities are replaced by two equations for vorticity. The first one is the definition of vorticity η $[\mathrm{s}^{-1}]$:

$$\eta=\frac{\partial v}{\partial x}-\frac{\partial u}{\partial y}.$$

The second vorticity equation follows from differentiating the previously stated shallow water equation for v with respect to x, and subtracting the differentiation of the equation for u with respect to y:

$$\frac{\partial}{\partial x}(\frac{\partial v}{\partial t} + (\vec{u}\cdot\nabla)v + \frac{rv}{H-h} - \nu\nabla^2 v)$$
$$-\frac{\partial}{\partial y}(\frac{\partial u}{\partial t} + (\vec{u}\cdot\nabla)u + \frac{ru}{H-h} - \nu\nabla^2 u) = \frac{\partial}{\partial x}((\vec{F}_p)_y) - \frac{\partial}{\partial y}((\vec{F}_p)_x) =$$
$$\frac{\partial}{\partial t}(\frac{\partial v}{\partial x} - \frac{\partial u}{\partial y}) + \frac{\partial u}{\partial x}(\frac{\partial v}{\partial x} - \frac{\partial u}{\partial y}) + \frac{\partial v}{\partial y}(\frac{\partial v}{\partial x} - \frac{\partial u}{\partial y})$$
$$+u(\frac{\partial^2 v}{\partial x^2} - \frac{\partial^2 u}{\partial x \partial y}) + v(\frac{\partial^2 v}{\partial x \partial y} - \frac{\partial^2 u}{\partial y^2}) - \nu\nabla^2(\frac{\partial v}{\partial x} - \frac{\partial u}{\partial y})$$
$$+\frac{r}{H-h}(\frac{\partial v}{\partial x} - \frac{\partial u}{\partial y}) + \frac{r}{(H-h)^2}(v\frac{\partial h}{\partial x} - u\frac{\partial h}{\partial y}) = -g\frac{\partial^2 \zeta}{\partial x \partial y} + g\frac{\partial^2 \zeta}{\partial x \partial y} =$$
$$\frac{\partial \eta}{\partial t} + (\frac{\partial u}{\partial x} + \frac{\partial v}{\partial y})\eta + u\frac{\partial \eta}{\partial x} + v\frac{\partial \eta}{\partial y} + \frac{r}{H-h}\eta + \frac{r}{(H-h)^2}(v\frac{\partial h}{\partial x} - u\frac{\partial h}{\partial y}) - \nu\nabla^2\eta = 0.$$

Then using the continuity equation yields the final form:

$$\frac{\partial \eta}{\partial t} + (\vec{u}\cdot\nabla)\eta + \frac{r}{H-h}\eta - \nu\nabla^2\eta + \frac{\eta}{H-h}(u\frac{\partial h}{\partial x} + v\frac{\partial h}{\partial y}) + \frac{r}{(H-h)^2}(v\frac{\partial h}{\partial x} - u\frac{\partial h}{\partial y}) = 0.$$

The main benefit of replacing the two equations for the currents (u, v) by the two vorticity equations is that now only once the friction and viscosity terms have to be calculated instead of twice. A disadvantage is that any lone uniform terms in the flow $\vec{u}$ just disappear in the vorticity equations, since in both equations only the spatial gradients of the currents appear. Only the non-uniform terms in the flow can be calculated using the vorticity equations.
The original depth-averaged shallow water equations are needed to calculate the uniform terms: suppose $\bar{u}$ is the uniform term of u, so $\frac{\partial \bar{u}}{\partial x} = 0$ and $\frac{\partial \bar{u}}{\partial y} = 0$. Plugging $\bar{u}$ into the the shallow water equation for along-channel velocity u gives:

$$\frac{\partial \bar{u}}{\partial t} + \frac{r\bar{u}}{H-h} = \overline{(\vec{F}_p)_x}.$$

Similiarly for any uniform part $\bar{v}$ of cross-channel velocity v:

$$\frac{\partial \bar{v}}{\partial t} + \frac{r\bar{v}}{H-h} = \overline{(\vec{F}_p)_y}.$$

Here, $\overline{\vec{F}_p}$ is the uniform part of $\vec{F}_p$.

2.2.3 Volumetric concentration equation

Next, for the concentration of sand in the water we use the following equation:

$$\frac{\partial C}{\partial t} + \nabla\cdot(\vec{u}C) - \nabla\cdot(\mu\nabla C + \mu\frac{w_s}{\kappa_v}\beta_b C\nabla h) = E - D.$$

Here, $C(\vec{x}, t)[\mathrm{m^3 m^{-2}}]$ is the depth-integrated volumetric sediment concentration, which indicates the total volume of sediment in the water column above a unit surface at (x, y). The terms $\nabla\cdot(\vec{u}C)$ describe advection of sediment by the water currents, while $\nabla\cdot(\mu\nabla C)$ describes the diffusion of sediment in the water, with $\mu[\mathrm{m^2 s^{-1}}]$ the horizontal eddy diffusivity coefficient. The complicated term $\nabla\cdot(\mu\frac{w_s}{\kappa_v}\beta_b C\nabla h)$ can be viewed as an 'delay'-term: it describes the settling and vertical diffusion of sediment in the water column. Here, $w_s[\mathrm{ms^{-1}}]$ is the settling velocity, which depends on -for example- the size of the sand

particles, and a higher w_s indicates that the in water suspended sand particles will drop faster to the bottom. The settling of sand is countered by the vertical diffusion of sand, which is described by the vertical eddy diffusivity coefficient $\kappa_v[\mathrm{m^2s^{-1}}]$. Lastly, β_b is the deposition parameter, which indicates that of the sand concentration C suspended in the water column a part $\beta_b C$ will be affected by these vertical interactions. All in all, this complicated term is a delay term for the suspended sand to settle, and this delay is caused by different vertical interactions within the water column. Note that this complicated parametrization is needed, since a two-dimensional model is used where vertical flows and gradients are not included. In Seminara & Tubino(2001) a three-dimensional model is used with a more intuitive volumetric concentration equation, which -however- leads to more complicated calculations.
On the right-hand side of the volumetric concentration equation the erosion $E[\mathrm{ms^{-1}}]$ and deposition $D[\mathrm{ms^{-1}}]$ of sediment is described. An amount $E = \alpha||\vec{u}||^2$ will become suspended sand in the water column, while an amount $D = \gamma C$ will leave the water column. Here $\alpha[\mathrm{sm^{-1}}]$ is the erosion parameter, and $\gamma[\mathrm{s^{-1}}]$ is the deposition parameter (not to be confused with the dimensionless β_b. The deposition parameter γ will be higher for faster settling sand (higher w_s) or more settling sand (higher β_b), while deposition will be slowed down if more vertical diffusion occurs (higher κ_v). Therefore, the deposition parameter γ can be described by $\gamma = w_s^2 \frac{\beta_b}{\kappa_v}$ [5].

2.2.4 Bed evolution equation

Lastly, but most importantly, the equation to describe the bed-evolution itself. This equation is the link between the tidal hydrodynamics and the actual sandy bed.

$$(1-p)\frac{\partial h}{\partial t} + \nabla \cdot < \vec{q_s} + \vec{q_b} >= 0$$

Here $\vec{q_s}[\mathrm{m^2s^{-1}}]$ is the transport of suspended sediment via the water, where $\vec{q_s} = \vec{u}C - \mu\nabla C - \mu\frac{w_s}{\kappa_v}\beta_b C\nabla h$. The advection of sand via water ($\vec{u}C$) is countered by the horizontal diffusion of sand in water (second term) and the delay term (third term) due to settling and vertical diffusion. Next, $\vec{q_b}[\mathrm{m^2s^{-1}}]$ is the transport of sediment as bed load. This is transport of sand 'rolling downhill': it is a damping term on the sandy bed causing sand from shoals to move towards lower troughs. It is described by $\vec{q_b} = -\hat{s}k_*||\vec{u}||^3\nabla h$, where $\hat{s}[\mathrm{s^2m^{-1}}]$ is the bed load transport constant and k_* the bed load bed slope parameter. The first parametrizes the importance of the flow ($||\vec{u}||^3$), while the latter parametrizes the importance of the bed steepness (∇h).
Now, $< \cdot >$ is the average over one tidal cycle with period $\frac{2\pi}{\sigma}$. Only the M_2-tide -the principal lunar semi-diurnal tide- is considered, which has a period of roughly twelve hours. So radial frequency $\sigma = 1.4 \cdot 10^{-4} s^{-1}$. The tidal average is:

$$< \cdot >= \frac{\sigma}{2\pi}\int_0^{\frac{2\pi}{\sigma}} \cdot \quad dt. \tag{1}$$

This is essential to the *flow over bed topography problem*. Since the bed generally evolves on a timescale of weeks to months, which is long compared to a tidal period, the bed pattern can be assumed to be constant for one tidal period. During one tidal period the bed will be insensitive to instantaneous rates of erosion and deposition. The bottom will only be described by the tidal averages of erosion and deposition.
Lastly, $p < 1$ is the porosity, and it indicates how well the sand on the bottom is 'packed'. If $1\mathrm{m}^3$ of sediment is deposited, then it will 'translate' to $\frac{1}{1-p}\mathrm{m}^3$ of sand on the bottom. For $p > 0$ the sand does not align perfectly, and is porous.

2.3 Flow over topography problem

One of the key elements of the model is the *flow over topography* feature. The bed is constant for a tidal period, and at the end the tidal averages of all physical interactions of the flow with the bed and the

resulting erosions and depositions are used to update the bed. In essence there are two time scales: the 'live' time scale, which is the physically accurate one in which $\vec{u}$, η and C operate, and the tidal time scale in which the bed h operates. To avoid confusion, the 'tidal time' will be indicated by τ instead of t, so the bed-evolution equation becomes:

$$(1-p)\frac{\partial h}{\partial \tau} = -\nabla \cdot < \vec{q_s} + \vec{q_b} >,$$

while the bed does not change 'live', so $\frac{\partial h}{\partial t} = 0$ from now on.
Because the bed evolution is calculated with tidal averages instead of 'live' values of erosion and deposition, an error will occur. After all, this is a deviation from physical reality. Luckily, Schramkowski et al (2002) found that the occurring error is negligible. The benefit of the different time scales is that it saves calculation time: sand that is washed away during flood and cancelled by returning sand during ebb will not be occurring in the bed update at all. More on the different time scales can be found in Van der Wegen et al.(2008).
All in all, the model functions as follows: a bed pattern $h(\vec{x})$ is given, then the corresponding live velocities, volumetric concentration and vorticity ($\vec{u}(\vec{x},t)$, $C(\vec{x},t)$ and $\eta(\vec{x},t)$) are calculated, and lastly the sediment transports $\vec{q_b}$ and $\vec{q_s}$ are determined. Finally, with the tidal averages the bed of the next tidal cycle can be found:

$$h(\tau) = h(\tau - \frac{2\pi}{\sigma}) \exp\left((-\frac{1}{1-p}\nabla \cdot < \vec{q_s} + \vec{q_b} >)(\frac{2\pi}{\sigma})\right).$$

This process can be repeated until the shoals are above the water surface ($h > H$), at which point the model is no longer valid. To simplify calculations further a morphological factor(MF) is added. In the model it is assumed that the bed change calculated for one tidal cycle is exactly repeated for another MF tidal cycles. This means that the bed changes are calculated for one cycle, then multiplied by a factor MF, and as a result the total bed evolution update for MF tidal cycles is calculated. So in essence in the model time-steps of MF tidal cycles are taken. Usually, MF = 730, which is equivalent to roughly one year. A visualization of this process can be seen in figure 5. So, given the bed at step i, then the bed changes are repeated MF times to get to step $i+1$, which is the same as a time-step of MF tidal cycles:

$$h|_{i+1} = h|_i * \left(\exp\left((-\frac{1}{1-p}\nabla \cdot < \vec{q_s} + \vec{q_b} >)(\frac{2\pi}{\sigma})\right)\right)^{\mathrm{MF}} = h|_i * \exp\left((-\frac{1}{1-p}\nabla \cdot < \vec{q_s} + \vec{q_b} >)(\frac{2\pi}{\sigma} * \mathrm{MF})\right).$$

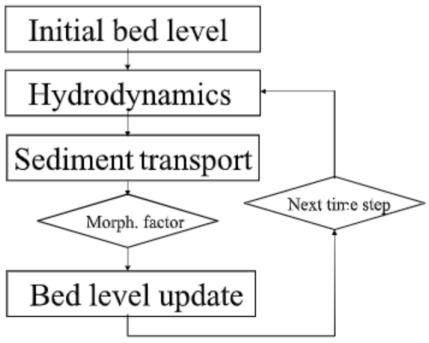

Figure 5: The update scheme of the sandy bed. Source: Van der Wegen & Roelvink (2008) [16].

2.4 Summary

All in all, the model consists of the continuity equation (2), vorticity equations (definition (3) and (4)) and volumetric concentration equation (5) to calculate $\vec{u}$, η and C given an initial bed topography h:

$$\nabla \cdot ((H-h)\vec{u}) = 0 \tag{2}$$

$$\eta = \frac{\partial v}{\partial x} - \frac{\partial u}{\partial y} \tag{3}$$

$$\frac{\partial \eta}{\partial t} + (\vec{u}\cdot\nabla)\eta + \frac{r}{H-h}\eta - \nu\nabla^2\eta + \frac{\eta}{H-h}(u\frac{\partial h}{\partial x} + v\frac{\partial h}{\partial y}) = -\frac{r}{(H-h)^2}(v\frac{\partial h}{\partial x} - u\frac{\partial h}{\partial y}) \tag{4}$$

$$\frac{\partial C}{\partial t} + \nabla\cdot(\vec{u}C) - \nabla\cdot(\mu\nabla C + \mu\frac{w_s}{\kappa_v}\beta_b C\nabla h) = E - D. \tag{5}$$

Since the boundaries of the channel are assumed to be solid and non-erodible, there can be neither water nor sediment transport through these. Therefore the following boundary conditions are imposed:

$$v = 0, \quad \frac{\partial C}{\partial y} = 0, \quad \frac{\partial h}{\partial y} = 0 \quad \text{and} \quad \frac{\partial u}{\partial y} = 0 \quad \text{at } y = 0, B \tag{6}$$

Furthermore, it is assumed that $\vec{u}$, C and η are finite. Lastly, the bed evolution equation, which is better known as the Exner-equation [15], with tidal time-scale τ:

$$(1-p)\frac{\partial h}{\partial \tau} = -\nabla\cdot < \vec{q_s} + \vec{q_b} > . \tag{7}$$

2.5 Parameter Values

All the parameters used in the model are summarized in table 1. Here, also the scaling of these parameters is given. Added is the amplitude of the tidal velocity U, which is assumed to be equal to the typical current velocity $\mathcal{U}$ in the channel. Also in the table are the straightforward scalings of vertical eddy diffusion (κ_v) with current velocity and undisturbed channel depth, of horizontal eddy viscosity ν with current velocity and channel width, and of horizontal eddy diffusion μ with current velocity and channel width. The intuition behind the formula for γ is already discussed, while the intuition behind $\beta_b = (1-e^{\frac{-w_s}{\kappa_v}H})^{-1}$ is similar: a higher settling velocity (w_s), lower vertical diffusion (κ_v) or a larger water column (H), will increase the amount of deposition, and hence will increase β_b, see also Hepkema et al.(2019). Lastly, the derivation for the linearized friction coefficient $r = \frac{8}{3\pi}c_d\mathcal{U}$, which scales with current velocity, can be found in Lorentz(1922), see [10] or [3].
The only characteristics which are different for each estuary, are the undisturbed depth, the channel width and the tidal velocity. In this study only four different estuaries are considered: the Western Scheldt, the Netarts Bay, and Exe estuary. Their characteristics are listed in table 2.

Table 1: Parameters and their value (range) after Hepkema et al.(2019)[5]

Parameter	value(s)	units	name
H	1.2-10	m	undisturbed water depth
B	800-7000	m	channel width
U	0.6-1	ms^{-}1	amplitude velocity of tide
$r = \frac{8}{3\pi} c_d \mathcal{U}$		ms^{-1}	friction coefficient
$\kappa_v = c_v \mathcal{U} H$		m^{2}s^{-1}	vertical eddy diffusion coefficient
$\nu = c_h^u \mathcal{U} B$		m^{2}s^{-1}	horizontal eddy viscosity coefficient
$\mu = c_h^c \mathcal{U} B$		ms^{-1}	horizontal eddy diffusion coefficient
$\mathcal{U} = U$		m^{2}s^{-1}	typical current velocity
$\gamma = \frac{w_s^2}{\kappa_v} \beta_b$		s^{-1}	deposition parameter
$\beta_b = (1 - e^{\frac{-w_s}{\kappa_v} H})^{-1}$			deposition parameter
g	9.81	ms$-$2	gravitational acceleration
σ	$1.4{\cdot}10^{-4}$	s^{-1}	frequency M_2-tide
w_s	0.013	ms^{-1}	settling velocity
α	$5{\cdot}10^{-6}$	s m^{-1}	erosion parameter
$\hat{s}$	$3{\cdot}10^{-4}$	s^{2}m^{-1}	bed load transport constant
p	0.4		porosity
c_d	0.0025		drag coefficient
p	2		bed load bed slope parameter
p	0.001		vertical diffusivity constant
p	0.001		horizontal diffusivity constant
c_h^u	0.001		horizontal viscosity constant

Table 2: Parameters and their value (range) after Hepkema et al.(2019)[5]

	B[km]	H[m]	U[ms^{-1}]
Western Scheldt	7.0	10.0	1.0
Exe estuary	1.0	2.6	0.6
Netarts Bay	0.8	1.2	0.6

3 Methods

3.1 Asymptotic analysis

Asymptotic analysis is a method to find approximate solutions to systems of differential equations. In this case, an equilibrium solution $(\vec{u}_0, \eta_0, C_0, h_0)$ is found for the channel system (equations (2) to (7)). Then a small disturbance is made to the bed: $h = h_0 + \epsilon h_1$. Here ϵ is a positive dimensionless variable. The disturbance is only of the first order in ϵ ($\mathcal{O}(\epsilon)$), while h_1 and h_0 have the same order of magnitude ($h_0 \sim h_1$). Just as in Van Veelen et al. (2018), ϵ is calculated via:

$$\epsilon = \frac{\max\limits_{(x,y)\in L\times B}(h_1)}{H} \tag{8}$$

It is imposed that $\epsilon < 1$, such that the shoals never grow above the water surface. Furthermore, the approximate solutions following asymptotic analysis are more reliable the smaller the disturbance parameter ϵ is, so ϵ is taken to be very small ($\epsilon \ll 1$).
The main idea of asymptotic analysis is to look at the effects the small disturbance ($\mathcal{O}(\epsilon)$) has on the other solutions $\vec{u}_0, \eta_0$ and C_0. These effects on the equilibrium solutions are studied at different orders of magnitude of ϵ: we look at the changes to $\vec{u}_0, \eta_0$ and C_0 in the linear regime ($\mathcal{O}(\epsilon)$), the second order regime ($\mathcal{O}(\epsilon^2)$) and the third order regime ($\mathcal{O}(\epsilon^3)$). This is done by expanding these relevant variables into powers of ϵ:

$$\begin{aligned} \vec{u} &= \vec{u}_0 + \epsilon\vec{u}_1 + \epsilon^2\vec{u}_2 + \epsilon^3\vec{u}_3 \\ \eta &= \eta_0 + \epsilon\eta_1 + \epsilon^2\eta_2 + \epsilon^3\eta_3 \\ C &= C_0 + \epsilon C_1 + \epsilon^2 C_2 + \epsilon^3 C_3, \end{aligned} \tag{9}$$

where $\vec{u}_0 \sim \vec{u}_1 \sim \vec{u}_2 \sim \vec{u}_3$, $\eta_0 \sim \eta_1 \sim \eta_2 \sim \eta_3$ and $C_0 \sim C_1 \sim C_2 \sim C_3$. Note that higher order terms (fourth order and higher) are not incorporated, simply to avoid too much calculations. These higher order terms are negligible as long as ϵ is very small. The analysis becomes more inaccurate for a larger ϵ.
Then these expansions, together with $h = h_0 + \epsilon h_1$, are plugged into the system (2) to (5). This will yield three different systems of differential equations, each for every order of ϵ. Given an initial bed h_0 with disturbance h_1, three solutions $(\vec{u}_i, \eta_i, C_i)$ ($i \in \{1, 2, 3\}$) can be found, and hence via equations (8) and (9) the approximate solutions $(\vec{u}, \eta, C)$ follow.
Finally, plugging the approximate expanded solutions together with $h = h_0 + \epsilon h_1$ into the bed evolution equation (7) yields the bed update for h_1. All in all, via asymptotic analysis the effects of the disturbance h_1 on the bed itself can be approximately found.
A more elaborate take on asymptotic analysis can be found in *Intro to Perturbation Methods* [6].

3.1.1 Equilibrium solution

As an equilibrium solution $(h_0, \vec{u}_0, \eta_0, C_0)$ to equations (2)-(7) a uniform flat bed is taken: $h_0 = 0$. Furthermore, the only current flow is the tidal current: $u_0 = U\cos\sigma t, v_0 = 0$, which the periodic flow in the along-channel direction with frequency σ. Both $\vec{u}_0$ and h_0 are spatially uniform, hence equation (2) is satisfied. From equation (3) follows $\eta_0 = 0$, which also satisfies equation (4).
Only the equilibrium volumetric concentration C_0 remains to be solved. Since the bed and current are spatially uniform the concentration C_0 also has to be spatially uniform: $C_0(\vec{x}, t) = C_0(t)$. Plugging this, together with $\vec{u}_0$ and h_0 into (5) yields:

$$\frac{dC_0}{dt} = E - D = \alpha(U\cos\sigma t)^2 - \gamma C_0.$$

Solving this differential equation yields:

$$C_0(t) = \frac{\alpha U^2}{2\gamma}\Big(1 + \frac{\gamma^2 \cos 2\sigma t + 2\gamma\sigma \sin 2\sigma t}{\gamma^2 + 4\sigma^2}\Big) + Ke^{-\gamma t}$$

with K an integration constant. Then demanding that the equilibrium solution is the same for every new tidal cycle ($C_0(t) = C_0(t + \frac{2\pi}{\sigma})$ yields $K = 0$. So:

$$C_0(t) = \frac{\alpha U^2}{2\gamma}\Big(1 + \frac{\gamma^2 \cos 2\sigma t + 2\gamma\sigma \sin 2\sigma t}{\gamma^2 + 4\sigma^2}\Big). \tag{10}$$

With a solution to the channel system the asymptotic analysis can now be continued.

3.1.2 Linearized system

To get to the first-order (linear) system of differential equations the expansions (9) and $h = h_0 + \epsilon h_1$ are plugged into the continuity equation (2), the vorticity equations ((3) and (4)) and the concentration equation (5). The solutions $h_0 = 0$ and $v_0 = 0$ are also plugged in to simplify the formulas. Next, all first-order terms ($\mathcal{O}(\epsilon)$) are collected. The first-order terms on the left-hand side of the equations must be equal to the first-order terms on the right-hand side, since ϵ is a dimensionless number that can take on any value in $(0, 1)$. The resulting system:

$$H\nabla \cdot \vec{u}_1 - u_0 \frac{\partial h_1}{\partial x} = 0 \tag{11}$$

$$\eta_1 = \frac{\partial v_1}{\partial x} - \frac{\partial u_1}{\partial y} \tag{12}$$

$$\frac{\partial \eta_1}{\partial t} + u_0 \frac{\partial \eta_1}{\partial x} + \frac{r}{H}\eta_1 - \nu\nabla^2\eta_1 = \frac{ru_0}{H^2}\frac{\partial h_1}{\partial y} \tag{13}$$

$$\frac{\partial C_1}{\partial t} + u_0 \frac{\partial C_1}{\partial x} + C_0(\nabla \cdot \vec{u}_1) - \mu\nabla^2 C_1 - \mu\frac{w_s}{\kappa_v}\beta_b C_0 \nabla^2 h_1 = E_1 - D_1 \tag{14}$$

with

$$\begin{cases} E_1 &= 2\alpha u_0 u_1 \\ D_1 &= \gamma C_1. \end{cases}$$

Note that given the initial bed disturbance h_1 the first-order variables $\vec{u}_1$, η_1 and C_1 can be determined. The derivation of the system is relatively straightforward by simply plugging in the expansions. Only the expansion of the friction term has to be dealt with via a Taylor-expansion. Under the assumption that $h \ll H$ follows:

$$\begin{aligned} \frac{ru}{H-h} &= \frac{ru}{H}\frac{1}{1-\frac{h}{H}} \\ &= \frac{ru}{H}(1 + \frac{h}{H} + (\frac{h}{H})^2 + (\frac{h}{H})^3 + ..) \\ &= \frac{r}{H}(u_0 + \epsilon u_1 + \epsilon^2 u_2 + \epsilon^3 u_3)(1 + \epsilon\frac{h_1}{H} + \epsilon^2(\frac{h_1}{H})^2 + \epsilon^3(\frac{h_1}{H})^3 + ..) \end{aligned}$$

and similar for the friction in the cross-channel direction.

3.1.3 Second-order system

A similar procedure holds for the second-order system. The expansions are plugged into the differential system and all second-order terms ($\mathcal{O}(\epsilon^2)$) are collected:

$$H\nabla\cdot\vec{u}_2 = h_1\nabla\cdot\vec{u}_1 + \vec{u}_1\cdot\nabla h_1 \tag{15}$$

$$\eta_2 = \frac{\partial v_2}{\partial x} - \frac{\partial u_2}{\partial y} \tag{16}$$

$$\begin{aligned}\frac{\partial\eta_2}{\partial t} + u_0\frac{\partial\eta_2}{\partial x} + \frac{r}{H}\eta_2 - \nu\nabla^2\eta_2 &= -\vec{u}_1\cdot\nabla\eta_1 + 2\frac{ru_0h_1}{H^3}\frac{\partial h_1}{\partial y} \\ &\quad - \frac{r}{H^2}(h_1\eta_1 + v_1\frac{\partial h_1}{\partial x} - u_1\frac{\partial h_1}{\partial y}) - \frac{u_0\eta_1}{H}\frac{\partial h_1}{\partial x}\end{aligned} \tag{17}$$

$$\begin{aligned}&\frac{\partial C_2}{\partial t} + u_0\frac{\partial C_2}{\partial x} + \vec{u}_1\cdot\nabla C_1 + C_0(\nabla\cdot\vec{u}_2) + C_1(\nabla\cdot\vec{u}_1) \\ &\quad -\mu\nabla^2C_2 - \mu\frac{w_s}{\kappa_v}\beta_bC_1\nabla^2h_1 - \mu\frac{w_s}{\kappa_v}\beta_b\nabla C_1\cdot\nabla h_1 = E_2 - D_2\end{aligned} \tag{18}$$

with

$$\begin{cases} E_2 &= 2\alpha u_0u_2 + \alpha||\vec{u}_1||^2 \\ D_2 &= \gamma C_2. \end{cases}$$

Now, given the initial bed disturbance h_1 and the first-order variables $\vec{u}_1$, η_1 and C_1 from the linear system, the second-order variables $\vec{u}_2$, η_2 and C_2 can be determined.

3.1.4 Third-order system

Lastly the third-order system: the expansions are plugged into the differential system and all third-order terms ($\mathcal{O}(\epsilon^3)$) are collected.

$$H\nabla\cdot\vec{u}_3 = h_1\nabla\cdot\vec{u}_2 + \vec{u}_2\cdot\nabla h_1 \tag{19}$$

$$\eta_3 = \frac{\partial v_3}{\partial x} - \frac{\partial u_3}{\partial y} \tag{20}$$

$$\begin{aligned}\frac{\partial\eta_3}{\partial t} + u_0\frac{\partial\eta_3}{\partial x} + \frac{r}{H}\eta_3 - \nu\nabla^2\eta_3 &= -\vec{u}_1\cdot\nabla\eta_2 + 3\frac{ru_0h_1}{H^4}\frac{\partial h_1}{\partial y} \\ &\quad - \frac{r}{H^3}(h_1^2\eta_1 + 2v_1h_1\frac{\partial h_1}{\partial x} - 2u_1h_1\frac{\partial h_1}{\partial y}) \\ &\quad - \frac{r}{H^2}(h_1\eta_2 + v_2\frac{\partial h_1}{\partial x} - u_2\frac{\partial h_1}{\partial y}) - \frac{u_0\eta_2}{H}\frac{\partial h_1}{\partial x} \\ &\quad - \frac{\eta_1}{H}(\vec{u}_1\cdot\nabla h_1 + h_1\nabla\cdot\vec{u}_1)\end{aligned} \tag{21}$$

$$\begin{aligned}&\frac{\partial C_3}{\partial t} + u_0\frac{\partial C_3}{\partial x} + \vec{u}_1\cdot\nabla C_2 + \vec{u}_2\cdot\nabla C_1 \\ &\quad +C_0(\nabla\cdot\vec{u}_3) + C_1(\nabla\cdot\vec{u}_2) + C_2(\nabla\cdot\vec{u}_1) \\ &-\mu\nabla^2C_3 - \mu\frac{w_s}{\kappa_v}\beta_bC_2\nabla^2h_1 - \mu\frac{w_s}{\kappa_v}\beta_b\nabla C_2\cdot\nabla h_1 = E_3 - D_3\end{aligned} \tag{22}$$

with

$$\begin{cases} E_3 &= 2\alpha u_0u_3 + 2\alpha(u_1u_2 + v_1v_2) \\ D_3 &= \gamma C_3. \end{cases}$$

At last the third-order variables $\vec{u}_3$, η_3 and C_3 can be calculated given the initial bed disturbance h_1 and the first-order variables $\vec{u}_1$, η_1 and C_1 from the linear system and the second-order variables $\vec{u}_2$, η_2 and C_2 from the second-order system.

3.1.5 Expanded bed evolution equation

Once $\vec{u}_j$ and C_j ($j \in \{1,2,3\}$) are known, current and volumetric concentration can be calculated. These, together with $h = h_0 + \epsilon h_1$, are plugged into the Exner equation (7) gives the bed-evolution equation up to third-order:

$$\begin{aligned}
(1-p)\frac{\partial h}{\partial \tau} &= -\nabla\cdot < \vec{q}_s + \vec{q}_b > = - < \nabla\cdot\vec{q}_s + \nabla\cdot\vec{q}_b > \\
&= - < \nabla\cdot(\vec{u}C - \mu\nabla C - \mu\frac{w_s}{\kappa_v}\beta_b C\nabla h) - \nabla\cdot\hat{s}k_*||\vec{u}||^3\nabla h > \\
&= - < \epsilon(C_0\nabla\cdot\vec{u}_1 + u_0\frac{\partial C_1}{\partial x} - \mu\nabla^2 C_1 - \mu\frac{w_s}{\kappa_v}\beta_b C_0\nabla^2 h_1) \\
&+ \epsilon^2(C_0\nabla\cdot\vec{u}_2 + C_1\nabla\cdot\vec{u}_1 + u_0\frac{\partial C_2}{\partial x} + \vec{u_1}\cdot\nabla C_1 - \mu\nabla^2 C_2 - \mu\frac{w_s}{\kappa_v}\beta_b\nabla C_1\cdot\nabla h_1 - \mu\frac{w_s}{\kappa_v}\beta_b C_1\nabla^2 h_1) \\
&+ \epsilon^3(C_0\nabla\cdot\vec{u}_3 + C_1\nabla\cdot\vec{u}_2 + C_2\nabla\cdot\vec{u}_1 + u_0\frac{\partial C_3}{\partial x} + \vec{u}_1\cdot\nabla C_2 + \vec{u}_2\cdot\nabla C_1 \\
&- \mu\nabla^2 C_3 - \mu\frac{w_s}{\kappa_v}\beta_b\nabla C_2\cdot\nabla h_1 - \mu\frac{w_s}{\kappa_v}\beta_b C_2\nabla^2 h_1) \\
&+ \epsilon(|u_0|^3) + \epsilon^2(3|u_0|u_1) + \epsilon^3(3|u_0|u_1^2 + 3u_0|u_0|u_2 + \frac{3}{2}|u_0|v_1^2) > \\
&= (1-p)\epsilon\frac{\partial h_1}{\partial \tau}
\end{aligned}$$

Finally, dividing both sides by ϵ gives the desired result.

3.2 Fourier analysis

To solve these three systems of differential equations Fourier analysis is used. First, the relevant variables are decomposed into spatial components.

$$\begin{aligned}
u_j &= \sum_{m=-M}^{m=M}\sum_{n=-N}^{N}\hat{u}_{jmn}\cos(l_n y)e^{ik_m x} \\
C_j &= \sum_{m=-M}^{m=M}\sum_{n=-N}^{N}\hat{C}_{jmn}\cos(l_n y)e^{ik_m x} \\
h_1 &= \sum_{m=-M}^{m=M}\sum_{n=-N}^{N}\hat{h}_{mn}\cos(l_n y)e^{ik_m x}
\end{aligned}$$

$$\begin{aligned}
v_j &= \sum_{m=-M}^{m=M}\sum_{n=-N}^{N}\hat{v}_{jmn}\sin(l_n y)e^{ik_m x} \\
\eta_j &= \sum_{m=-M}^{m=M}\sum_{n=-N}^{N}\hat{\eta}_{jmn}\sin(l_n y)e^{ik_m x}.
\end{aligned}$$

As wave-number in the cross-channel direction $l_n = \frac{\pi n}{B}[\mathrm{m}^{-1}]$ is used, while the along-channel wave-number is $k_m = \frac{2\pi m}{L}[\mathrm{m}^{-1}]$. Note that there are $2M+1$ modes in the along-channel direction and $2N+1$ modes in the cross-channel direction. To get an exact solution one needs $M, N \longrightarrow \infty$. In this thesis usually $M, N \leq 10$ is used, so -again- the Fourier analysis will be an approximation. In Schramkowski et al.(2004) a validation is given for expanding the bed into spatial modes.

The expansion in either cosines or sines is used as a convenience: the solutions now automatically satisfy the boundary conditions (6). The components -for example $\hat{u}_j mn$- refer to the (m, n) spatial mode and may be complex. The solutions themselves however must be real. Therefore, for $u_j \in \mathbb{R}$ it is needed that $\hat{u}^*_{j,m,n} = \hat{u}_{j,-m,n}$, and similar for the others.
Next, the spatial components are also expanded into temporal Fourier coefficients, where multiples of frequency σ are used for convenience:

$$(\hat{u}_{jmn}, \hat{v}_{jmn}, \hat{\eta}_{jmn}, \hat{C}_{jmn}, \hat{h}_{mn}) = \sum_{p=-P}^{P} (U_{jmnp}, V_{jmnp}, E_{jmnp}, C_{jmnp}, H_{1mnp}) e^{ip\sigma t}.$$

As a note regarding the Fourier-expansion: the temporal expansion ends at $P = 2$. This means that effects with the tidal frequency (frequency σ, M_2-tide) and subtidal effects (frequency 2σ, M_4-effects) are included, but no effects with higher frequencies. This is based on Olabarrieta el al.(2017)[11]. In this paper funnel-shaped estuaries are studied using a non-linear three-dimensional model. It was found that tidal and subtidal currents are relevant and sufficient in the morphological evolution of the tidal bars.
Furthermore, since the bed and its disturbance h_1 are constant on the live timescale t: $H_{1mnp} = 0$ for $p \neq 0$ and $H_{1mn0} = \hat{h}_{mn}$. Also, sand has to be conserved in the system, since no sand can escape through the boundaries. Hence:

$$0 = \frac{d}{d\tau} \int_{B\times L} h_1(x, y) dx dy = \frac{d}{d\tau} (\hat{h_{00}} BL).$$

So $\hat{h_{00}}$ has to be constant: the whole bed cannot rise (or fall) everywhere. For convenience $\hat{h_{00}} = 0$ is taken. Lastly, since the bed is expressed as a cosine-series the amplitude $\hat{h}_{m,-n}$ results in the same bed topography as $\hat{h}_{m,n}$. All in all, when plotting amplitudes the results for $\hat{h}_{m,-n}$ are added to $\hat{h}_{m,n}$.

3.2.1 Convolutions

In this section some convolution functions are defined. When one Fourier series is multiplied by another the convolution function defines the components of the new resulting Fourier series. There are three cases.

Since $\cos\alpha \sin\beta = \frac{1}{2}(\sin\alpha + \beta + \sin\beta - \alpha)$ it follows that:

$$\cos(\beta)\sin(n-\beta) = \frac{1}{2}\sin(n) + \frac{1}{2}\sin(n-2\beta)$$
$$\cos(\beta)\sin(n+\beta) = \frac{1}{2}\sin(n) + \frac{1}{2}\sin(n+2\beta).$$

Furthermore, it is straightforward that $e^{\beta} e^{m-\beta} = e^m$. So:

$$\left(\sum_m \sum_n \sum_p A_{mnp} \cos(l_n y) e^{i(k_m x + p\sigma t)}\right)\left(\sum_m \sum_n \sum_p B_{mnp} \sin(l_n y) e^{i(k_m x + p\sigma t)}\right)$$
$$= \sum_m \sum_n \sum_p (A \star B)^{cs}_{mnp} \sin(l_n y) e^{i(k_m x + p\sigma t)}$$

where

$$(A \star B)^{cs}_{mnp} = \sum_a \sum_b \sum_c \frac{1}{2} A_{abc} (B_{m-a,n-b,p-c} + B_{m-a,n+b,p-c})$$

This means that the spatial mode (a, b) (from the cosine) and the modes $(m - a, n \pm b)$ (from the sine) interact to form a (m, n)-mode. Note that it matters which contribution came from the sine-series and which from the cosine-series: their order matters, since $\cos\alpha \sin\beta \neq \cos\beta \sin\alpha$.

Next, with $\cos\alpha\cos\beta = \frac{1}{2}(\cos\alpha+\beta + \cos\alpha-\beta)$ follows that:

$$\cos(\beta)\cos(n-\beta) = \frac{1}{2}\cos(n) + \frac{1}{2}\cos(n-2\beta)$$
$$\cos(\beta)\cos(n+\beta) = \frac{1}{2}\cos(n) + \frac{1}{2}\cos(n+2\beta).$$

So likewise,

$$\Big(\sum_m\sum_n\sum_p A_{mnp}\cos(l_n y)e^{i(k_m x+p\sigma t)}\Big)\Big(\sum_m\sum_n\sum_p B_{mnp}\cos(l_n y)e^{i(k_m x+p\sigma t)}\Big)$$
$$= \sum_m\sum_n\sum_p (A\star B)^{cc}_{mnp}\cos(l_n y)e^{i(k_m x+p\sigma t)}$$

where

$$(A\star B)^{cc}_{mnp} = \sum_a\sum_b\sum_c \frac{1}{2}A_{abc}(B_{m-a,n-b,p-c} + B_{m-a,n+b,p-c}) \text{ for } n\geq 0$$

and $(A\star B)^{cc}_{mnp} = 0$ for $n<0$

Again spatial mode (a,b) interacts with spatial modes $(m-a, n\pm b)$ to form (m,n). All the contributions are projected onto the non-negative modes $(n\geq 0)$. Physically it does not matter, since $\cos l_{-n}y = \cos l_n y$. Note, that the order of A, B does not matter, since $\cos\alpha\cos\beta = \cos\beta\cos\alpha$ then $(A\star B)^{cc} = (B\star A)^{cc}$.

Lastly, for the sine-sine interaction the product formula $\sin\alpha\sin\beta = \frac{1}{2}(-\cos\alpha+\beta + \cos\alpha-\beta)$ is used:

$$\sin(\beta)\sin(n-\beta) = -\frac{1}{2}\cos(n) + \frac{1}{2}\cos(n-2\beta)$$
$$\sin(\beta)\sin(n+\beta) = \frac{1}{2}\cos(n) - \frac{1}{2}\cos(n+2\beta).$$

So likewise,

$$\Big(\sum_m\sum_n\sum_p A_{mnp}\sin(l_n y)e^{i(k_m x+p\sigma t)}\Big)\Big(\sum_m\sum_n\sum_p B_{mnp}\sin(l_n y)e^{i(k_m x+p\sigma t)}\Big)$$
$$= \sum_m\sum_n\sum_p (A\star B)^{ss}_{mnp}\cos(l_n y)e^{i(k_m x+p\sigma t)}$$

where

$$(A\star B)^{ss}_{mnp} = \sum_a\sum_b\sum_c \frac{1}{2}A_{abc}(-B_{m-a,n-b,p-c} + B_{m-a,n+b,p-c}) \text{ for } n\geq 0$$

and $(A\star B)^{ss}_{mnp} = 0$ for $n<0$

Like before modes (a,b) and $(m-, n\pm b)$ interact to form (m,n). All contributions are projected onto non-negative $n\geq 0$, since the result is a cosine-series with $\cos l_{-n}y = \cos l_n y$. And similar to the cosine-cosine interaction: the order of A, B does not matter.

A final note, when writing - for example- $(kA\star lB)^{cs}_{mnp}$ then it is defined as
$\sum_a\sum_b\sum_c \frac{1}{2}k_a A_{abc}(l_{n-b}B_{m-a,n-b,p-c} + l_{n+b}B_{m-a,n+b,p-c})$.

3.2.2 Fourier-expansion linear system

Applying Fourier analysis to the linear system yields:

$$\begin{aligned}
ik_m H U_{1mnp} + H l_n V_{1mnp} &= i\frac{U}{2}(H_{1,m,n,p-1} + H_{1,m,n,p+1}) \\
E_{1mnp} &= ik_m V_{1mnp} + l_n U_{1mnp} \\
(i\sigma p + \frac{r}{H} + \nu(k_m^2 + l_n^2))E_{1mnp} + i\frac{Uk_m}{2}(E_{1,m,n,p-1} + E_{1,m,n,p+1}) &= \frac{-Ur}{2H^2} l_n (H_{1,m,n,p-1} + H_{1,m,n,p+1}) \\
(i\sigma p + \mu(k_m^2 + l_n^2) + \gamma)C_{1mnp} + i\frac{Uk_m}{2}(C_{1,m,n,p-1} + C_{1,m,n,p+1}) &= -\mu\frac{w_s}{\kappa_v}\beta_b(k_m^2 + l_n^2)C_{0p}h_1\hat{}mn \\
-\alpha U(U_{1,m,n,p-1} + U_{1,m,n,p+1}) + ik_m(C_0 \star U_{1mn})_p + l_n(C_0 \star V_{1mn})_p &
\end{aligned}$$

where C_{0p} is the pth temporal Fourier component of $C_0 = \sum_{p=-P}^{P} C_{0p} e^{ip\sigma t}$ and the convolution is defined as $(C_0 \star U_{1mn})_p = \sum_c C_{0c} U_{1,m,n,p-c}$. Note that this system is undetermined for $(m, n) = (0, 0)$.
For the uniform solution ($(0,0)$-mode) the Fourier-analysis of the original shallow-water equations are needed:

$$\begin{aligned}
(i\sigma p + \frac{r}{H})U_{100p} + \frac{rU}{2H^2} &= 0 \\
V_{100p} &= 0 \\
E_{100p} &= 0 \\
(i\sigma p + \gamma)C_{100p} - \alpha U(C_{1,0,0,p-1} + C_{1,0,0,p+1}) &= 0.
\end{aligned}$$

3.2.3 Fourier-expansion second-order system

For the second-order system the Fourier analysis gives:

$$\begin{aligned}
ik_m H U_{2mnp} + H l_n V_{2mnp} &= F_{mnp} \\
E_{2mnp} &= ik_m V_{2mnp} + l_n U_{2mnp} \\
(i\sigma p + \frac{r}{H} + \nu(k_m^2 + l_n^2))E_{2mnp} + i\frac{Uk_m}{2}(E_{2,m,n,p-1} + E_{2,m,n,p+1}) &= B_{mnp} \\
(i\sigma p + \mu(k_m^2 + l_n^2) + \gamma)C_{2mnp} + i\frac{Uk_m}{2}(C_{2,m,n,p-1} + C_{2,m,n,p+1}) &= D_{mnp} \\
-\alpha U(U_{2,m,n,p-1} + U_{2,m,n,p+1}) + ik_m(C_0 \star U_{2mn})_p + l_n(C_0 \star V_{2mn})_p &
\end{aligned}$$

where

$$\begin{aligned}
F_{mnp} &= i(H_1 \star kU_1)^{cc}_{mnp} + (H_1 \star lV_1)^{cc}_{mnp} + i(kH_1 \star U_1)^{cc}_{mnp} - (lH_1 \star V_1)^{ss}_{mnp} \\
B_{mnp} &= -i(U_1 \star kE_1)^{cs}_{mnp} - (lE_1 \star V_1)^{cs}_{mnp} - \frac{r}{H^3}U((H_1 \star lH_1)^{cs}_{m,n,p-1}) + (H_1 \star lH_1)^{cs}_{m,n,p+1})) \\
&\quad - \frac{r}{H^2}((H_1 \star E_1)^{cs}_{mnp}) + i(kH_1 \star V_1)^{cs}_{mnp}) + (U_1 \star lH_1)^{cs}_{mnp})) \\
&\quad - \frac{iU}{2H}((kH_1 \star E_1)^{cs}_{m,n,p-1}) + (kH_1 \star E_1)^{cs}_{m,n,p+1})) \\
D_{mnp} &= -i(U_1 \star kC_1)^{cc}_{mnp} + (V_1 \star lC_1)^{ss}_{mnp} - i(C_1 \star kU_1)^{cc}_{mnp} - (C_1 \star lV_1)^{cc}_{mnp} \\
&\quad - \mu\frac{w_s}{\kappa_v}\beta_b(C_1 \star (k^2 + l^2)H_1)^{cc}_{mnp} - \mu\frac{w_s}{\kappa_v}\beta_b((kC_1 \star kH_1)^{cc}_{mnp} - (lC_1 \star lH_1)^{ss}_{mnp}) \\
&\quad + \alpha((U_1 \star U_1)^{cc}_{mnp}) + (V_1 \star V_1)^{ss}_{mnp}).
\end{aligned}$$

The uniform parts are the solution of:

$$
\begin{aligned}
(i\sigma p+\frac{r}{H})U_{200p}+i(U_1\star kU_1)^{cc}_{00p}-(V_1\star lU_1)^{ss}_{00p}+\frac{rU}{2H^3}((H_1\star H_1)^{cc}_{0,0,p-1}+(H_1\star H_1)^{cc}_{0,0,p+1}) \\
+\frac{r}{H^2}(U_1\star H_1)^{cc}_{0,0,p}=0 \\
(i\sigma p+\frac{r}{H})V_{200p}+i(U_1\star kV_1)^{cs}_{00p}+(lV_1\star V_1)^{cs}_{00p}+\frac{r}{H^2}(H_1\star V_1)^{cs}_{0,0,p}=0 \\
E_{200p}=0 \\
(i\sigma p+\gamma)C_{200p}-\alpha U(C_{2,0,0,p-1}+C_{2,0,0,p+1})=D_{00p}.
\end{aligned}
$$

3.2.4 Fourier-expansion third-order system

And finally for the third-order system:

$$
\begin{aligned}
ik_mHU_{3mnp}+Hl_nV_{3mnp}&=G_{mnp} \\
E_{3mnp}&=ik_mV_{3mnp}+l_nU_{3mnp} \\
(i\sigma p+\frac{r}{H}+\nu(k_m^2+l_n^2))E_{3mnp}+i\frac{Uk_m}{2}(E_{3,m,n,p-1}+E_{3,m,n,p+1})&=P_{mnp} \\
(i\sigma p+\mu(k_m^2+l_n^2)+\gamma)C_{3mnp}+i\frac{Uk_m}{2}(C_{3,m,n,p-1}+C_{3,m,n,p+1})&=Q_{mnp} \\
-\alpha U(U_{3,m,n,p-1}+U_{3,m,n,p+1})+ik_m(C_0\star U_{3mn})_p+l_n(C_0\star V_{3mn})_p&
\end{aligned}
$$

where

$$
\begin{aligned}
G_{mnp}&=i(H_1\star kU_2)^{cc}_{mnp}+(H_1\star lV_2)^{cc}_{mnp}+i(kH_1\star U_2)^{cc}_{mnp}-(lH_1\star V_2)^{ss}_{mnp} \\
P_{mnp}&=-i(U_1\star kE_2)^{cs}_{mnp}-(lE_2\star V_1)^{cs}_{mnp}-i(U_2\star kE_1)^{cs}_{mnp}-(lE_1\star V_2)^{cs}_{mnp} \\
&\quad-\frac{3rU}{2H^4}((H_1\star(H_1\star lH_1)^{cs})^{cs}_{m,n,p-1})+(H_1\star(H_1\star lH_1)^{cs})^{cs}_{m,n,p+1})) \\
&\quad-\frac{r}{H^3}((H_1\star(H_1\star E_1)^{cs})^{cs}_{mnp})+2i(H_1\star(kH_1\star V_1)^{cs})^{cs}_{mnp})+2(H_1\star(U_1\star lH_1)^{cs})^{cs}_{mnp})) \\
&\quad-\frac{r}{H^2}((H_1\star E_2)^{cs}_{mnp})+i(kH_1\star V_2)^{cs}_{mnp})+(U_2\star lH_1)^{cs}_{mnp})) \\
&\quad-\frac{1}{H}(i((U_1\star kH_1)^{cc}\star E_1)^{cs}_{mnp})-((V_1\star lH_1)^{ss}\star E_1)^{cs}_{mnp}) \\
&\quad+i((H_1\star kU_1)^{cc}\star E_1)^{cs}_{mnp})+((H_1\star lV_1)^{cc}\star E_1)^{cs}_{mnp})) \\
Q_{mnp}&=-i(U_1\star kC_2)^{cc}_{mnp}+(V_1\star lC_2)^{ss}_{mnp}-i(U_2\star kC_1)^{cc}_{mnp}+(V_2\star lC_1)^{ss}_{mnp} \\
&\quad-i(C_1\star kU_2)^{cc}_{mnp}-(C_1\star lV_2)^{cc}_{mnp}-i(C_2\star kU_1)^{cc}_{mnp}-(C_2\star lV_1)^{cc}_{mnp} \\
&\quad-\mu\frac{w_s}{\kappa_v}\beta_b(C_2\star(k^2+l^2)H_1)^{cc}_{mnp}-\mu\frac{w_s}{\kappa_v}\beta_b((kC_2\star kH_1)^{cc}_{mnp}-(lC_2\star lH_1)^{ss}_{mnp}) \\
&\quad+2\alpha((U_1\star U_2)^{cc}_{mnp})+(V_1\star V_2)^{ss}_{mnp}).
\end{aligned}
$$

The uniform parts are the solution of:

$$\begin{aligned}
(i\sigma p+\frac{r}{H})U_{300p}+i(U_1\star kU_2)^{cc}_{00p}-(V_1\star lU_2)^{ss}_{00p}+i(U_2\star kU_1)^{cc}_{00p}-(V_2\star lU_1)^{ss}_{00p}\\
+\frac{rU}{2H^4}(((H_1\star H_1)^{cc}\star H_1)^{cc}_{0,0,p-1}+((H_1\star H_1)^{cc}\star H_1)^{cc}_{0,0,p+1})\\
+\frac{r}{H^3}((U_1\star H_1)^{cc}\star H_1)^{cc}_{0,0,p}+\frac{r}{H^2}(U_2\star H_1)^{cc}_{0,0,p}=0\\
+(i\sigma p+\frac{r}{H})V_{300p}+i(U_1\star kV_2)^{cs}_{00p}-(lV_2\star lU_2)^{cs}_{00p}+i(U_2\star kV_1)^{cs}_{00p}+(lV_1\star V_2)^{cs}_{00p}\\
+\frac{r}{H^3}((H_1\star H_1)^{cc}\star V_1)^{cs}_{0,0,p}+\frac{r}{H^2}(H_1\star V_2)^{cs}_{0,0,p}=0\\
E_{300p}=0\\
(i\sigma p+\gamma)C_{300p}-\alpha U(C_{3,0,0,p-1}+C_{3,0,0,p+1})=Q_{00p}.
\end{aligned}$$

3.2.5 Fourier-expansion bed evolution equation

Lastly, the Fourier-series are plugged into the bed-evolution equation for h_1. Important here is that the tidal-average is taken, which only causes the zeroth temporal Fourier coefficient to remain:

$$<\sum_p A_p e^{ip\sigma t}>=\sum_p \frac{\sigma}{2\pi}A_p\int_0^{\frac{2\pi}{\sigma}} e^{ip\sigma t}dt=A_0.$$

The resulting evolution equation for every $\hat{h}_{mn}$-amplitude:

$$\begin{aligned}
(1-p)\frac{d\hat{h}_{mn}}{d\tau}&=ik_m(C_0\star U_{1mn})_0+l_n(C_0\star V_{1mn})_0+\frac{ik_mU}{2}(C_{1,m,n,-1}+C_{1,m,n,1})\\
&+\mu(k_m^2+l_n^2)C_{1mn0}+\mu\frac{w_s}{\kappa_v}\beta_bC_{0,0}(k_m^2+l_n^2)\hat{h}_{mn}\\
&\epsilon(ik_m(C_0\star U_{2mn})_0+l_n(C_0\star V_{2mn})+i(C_1\star kU_1)^{cc}_{mn0}+(C_1\star lV_1)^{cc}_{mn0}+i(U_1\star kC_1)^{cc}_{mn0}\\
&-(V_1\star lC_1)^{ss}_{mn0}+\frac{iUk_m}{2}(C_{2,m,n,-1}+C_{2,m,n,1})+\mu(k_m^2+l_n^2)C_{2mn0}\\
&+\mu\frac{w_s}{\kappa_v}\beta_b((kC_1\star kH_1)^{cc}_{mn0}-(lC_1\star lH_1)^{ss}_{mn0}+(C_1\star(k^2+l^2)H_1)^{cc}_{mn0}))\\
&+\epsilon^2(ik_m(C_0\star U_{3mn})_0+l_n(C_0\star V_{3mn})+i(C_1\star kU_2)^{cc}_{mn0}+(C_1\star lV_2)^{cc}_{mn0}\\
&+i(C_2\star kU_1)^{cc}_{mn0}+(C_2\star lV_1)^{cc}_{mn0}+i(U_2\star kC_1)^{cc}_{mn0}-(V_2\star lC_1)^{ss}_{mn0}\\
&+\frac{iUk_m}{2}(C_{3,m,n,-1}+C_{3,m,n,1})+\mu(k_m^2+l_n^2)C_{3mn0}\\
&+\mu\frac{w_s}{\kappa_v}\beta_b((kC_2\star kH_1)^{cc}_{mn0}-(lC_2\star lH_1)^{ss}_{mn0}+(C_2\star(k^2+l^2)H_1)^{cc}_{mn0}))\\
&+\hat{s}k_*\frac{4U^3}{3\pi}(k_m^2+l_n^2)\hat{h}_{mn}\\
&+\epsilon\hat{s}k_*((k\Phi\star kH_1)^{cc}_{mn}+(\Phi\star k^2H_1)^{cc}_{mn}-(l\Phi\star lH_1)^{ss}_{mn}+(\Phi\star l^2H_1)^{cc}_{mn})\\
&+\epsilon^2\hat{s}k_*((k\Xi\star kH_1)^{cc}_{mn}+(\Xi\star k^2H_1)^{cc}_{mn}-(l\Xi\star lH_1)^{ss}_{mn}+(\Xi\star l^2H_1)^{cc}_{mn}).
\end{aligned}$$

Where is defined:

$$\begin{aligned}
<||\vec{u}||^3>&=<|u_0|^3>+\epsilon<3|u_0|u_1>+\epsilon^2<3|u_0|u_1^2+3u_0|u_0|u_2+\frac{3}{2}|u_0|v_1^2>\\
&=\frac{4U^3}{3\pi}+\epsilon\sum_{m,n}\Phi_{m,n}\cos(l_ny)e^{ik_mx}+\epsilon^2\sum_{m,n}\Xi_{m,n}\cos(l_ny)e^{ik_mx},
\end{aligned}$$

where

$$\Phi_{mn} = \frac{3U^2}{2\pi} \sum_j \big((\frac{1}{4j+1} - \frac{2}{4j+3} + \frac{1}{4j+5}) U_{1,m,n,4j+3} - (\frac{1}{4j-1} - \frac{2}{4j+1} + \frac{1}{4j+3}) U_{1,m,n,4j+1} \big)$$

$$\begin{aligned}
\Xi_{mn} = & \\
& \frac{3U}{2} \sum_j ((\frac{1}{4j+1} - \frac{2}{4j+3} + \frac{1}{4j+5})(U_1 \star U_1)^{cc}_{m,n,4j+3} - (\frac{1}{4j-1} - \frac{2}{4j+1} + \frac{1}{4j+3})(U_1 \star U_1)^{cc}_{m,n,4j+1} \\
& + \frac{3U}{2\pi} \sum_j ((\frac{1}{4j+1} - \frac{2}{4j+3} + \frac{1}{4j+5})(V_1 \star V_1)^{ss}_{m,n,4j+3} - (\frac{1}{4j-1} - \frac{2}{4j+1} + \frac{1}{4j+3})(V_1 \star V_1)^{ss}_{m,n,4j+1} \\
& + \frac{3U^2}{2\pi} \sum_j (\frac{1}{4j+1} - \frac{2}{4j+3} + \frac{1}{4j+5}) U_{2,m,n,4j+3} - (\frac{1}{4j-1} - \frac{2}{4j+1} + \frac{1}{4j+3}) U_{2,m,n,4j+1}.
\end{aligned}$$

Finally, these systems are put into *Python*-code to calculate the (approximate) current and concentration in the channel. Then, together with equation (8) the differential equation for the bed evolution is solved.

4 Linear system results & discussion

When only using the linear system to simulate the bed evolution some striking features are already observed. Each amplitude $|\hat{h}_{mn}|$ experiences either exponential growth or decay, as can be seen in figure 6 of the amplitude-evolutions. Note that modes with $m < 0$ are excluded here: they are just the complex conjugate of modes with $m < 0$. Furthermore, the amplitudes do not interact at all: they continue their exponential path from the start without ever changing course and regardless of the initial starting value of the amplitude.
In figure 7 the different exponential growth rates $\omega_{mn}(\mathrm{s}^{-1})$ belonging to the amplitudes of the Western Scheldt are plotted. This figure is in accordance with the results from Hepkema et al.(2019), so this confirms the linear system calculations are functioning properly. Note that modes (m, n) with $\omega_{mn} > 0$ are unstable, so in figure 6 these are the modes $(2, 2), (1, 1), (1, 2)$. This also confirms the findings by Seminara & Tubino (2001) that even in a nearly flat bed instability occurs, which eventually grows to form the tidal bars. Other modes have $\omega_{mn} < 0$, and they decay to zero. Note that on the horizontal axis of figure wave-number k_m is plotted as a continuous variable k: the rate ω is calculated for different wave-numbers k_m by varying the section length L. This level of freedom is not available at the second- or third-order system. The length L that is chosen in these higher-order systems is such that the dominant (largest) wave-mode can fit an integer-times lengthwise in the channel. This way the dominant wave-number is certain to be present in the simulated channel section.
The dominant wave-mode (m, n) is the mode with the largest growth rate ω_{mn}: in figure 7 this would be the mode corresponding to $k_m = 0.45\mathrm{km}^{-1}$ and $n = 2$. Since this wave-mode grows the fastest, after 50 years the bed has already the associated (m, n)-pattern. This dominant, or preferential mode will hence be expected to be the main pattern in real-life estuary, and one would expect the Western Scheldt to have tidal bars with $k_m = 0.45\mathrm{km}^{-1}$ and $n = 2$. For the Western Scheldt a section with $L = 25\mathrm{km}$ is taken, so that that the dominant longitudinal wave fits exactly twice into the section: $\frac{25\mathrm{km}0.45\mathrm{km}^{-1}}{2\pi} \approx 2$. Therefore, the dominant mode in the Western Scheldt is $(2, 2)$, see the channel section in figure 8.
Although non-linear effects or realistic erodible walls are not present, the preferential wave-mode predicted by the crude approximation has reasonable agreement with the observed tidal bar lengths and widths in estuaries, see Hepkema et al. (2019). Hence, the dominant wave-mode is the most important: it determines the main pattern of estuaries.
Another key features observed by Hepkema et al.(2019), but reproduced here, is the effect of different channel widths and depths. When increasing the depth, or narrowing the channel causes the preferential mode to have lower mode-numbers: the tidal bar wavelengths in cross- and along-channel direction become larger. This has also been observed empirically by Leuven et al.(2016). Moreover, in a narrow, deep channel fewer modes are unstable. For example, one can see in figure 10 that for the narrower Exe estuary $(1, 1)$ is the dominant mode instead of $(2, 2)$ from the Western-Scheldt, also see the associated ω-curves of the Exe estuary in figure 9. Narrowing and deepening can be done such that only very few modes are actually unstable. This is a near-critical situation, see for example the ω-curves in figure 24.
Where the linear system fails, is that the unstable modes keep growing exponentially: they eventually grow above the water surface, and at this point the model is no longer valid.

4.1 Mathematical interpretation

Looking at the Fourier-analyzed linear system in section 3.2.2 one can see an important mathematical characteristic: every term is linearly dependent on a Fourier-component of either the current, vorticity, concentration or the bed-disturbance. This means that the (m, n)-components of the current, vorticity, concentration and bed are all linearly dependent on each other. This implies that different spatial modes do not interact with each other: there are no convolutions. This explains why all amplitudes just 'run their course' without being influenced by the others.

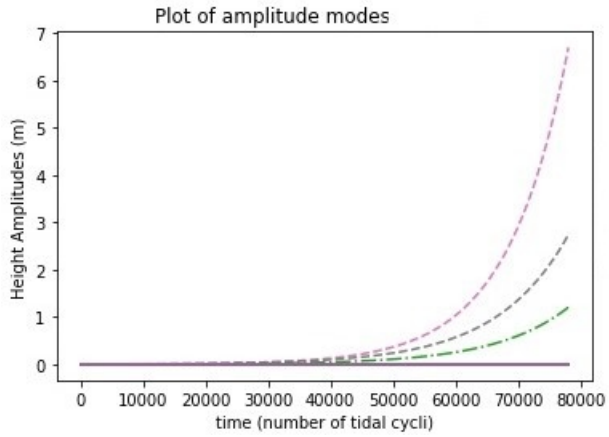

Figure 6: Amplitude evolution in Western Scheldt for linear system. Unstable modes $(2,2)$(pink), $(1,1)$ (gray) and $(1,2)$(green), where $L = 25km$ is used.

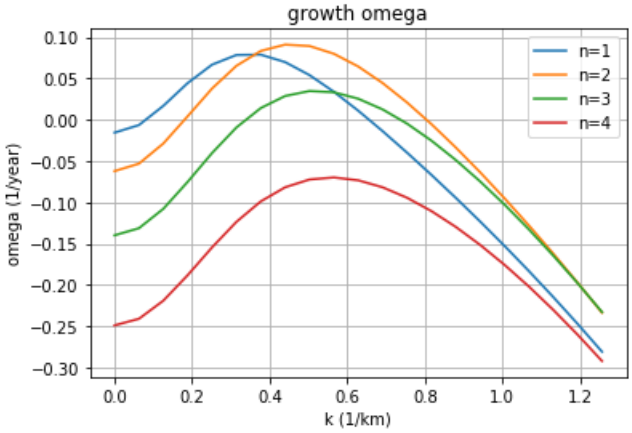

Figure 7: The ω-curves for the Western Scheldt.

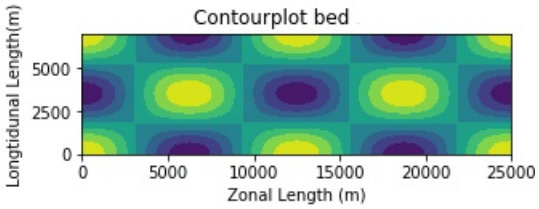

Figure 8: The associated bed pattern for the Western Scheldt with the linear system: dominated by the $(2,2)$-mode.

This also implies that the (m,n)-components of the current, vorticity and concentration are linearly dependent on the bed-disturbance amplitude $\hat{h}_{mn}$, so one can write:

$$(\hat{u}_{1mn}, \hat{v}_{1mn}, \hat{\eta}_{1mn}, \hat{C}_{1mn}) = \hat{h}_{mn} \sum_{p=-P}^{P} (U_{1mnp}, V_{1mnp}, E_{1mnp}, C_{1mnp}) e^{ip\sigma t}.$$

Plugging this into the linear part of the bed-evolution equation in section 3.1.5, yields (see also Hepkema et al.(2019)):

$$\begin{aligned}(1-p)\frac{d\hat{h}_{mn}}{d\tau} &= (ik_m(C_0 \star U_{1mn})_0 + l_n(C_0 \star V_{1mn})_0)\hat{h}_{mn} + \frac{ik_m U}{2}(C_{1,m,n,-1} + C_{1,m,n,1})\hat{h}_{mn} \\ &+ \mu(k_m^2 + l_n^2)C_{1mn0}\hat{h}_{mn} + \mu\frac{w_s}{\kappa_v}\beta_b C_{0,0}(k_m^2 + l_n^2)\hat{h}_{mn} \\ &+ \hat{s}k_*\frac{4U^3}{3\pi}(k_m^2 + l_n^2)\hat{h}_{mn}.\end{aligned}$$

Now, since $C_{0,p} = 0$ for $p \notin \{0, \pm 2\}$ (see expression (10)), and using the continuity equation from the linear system (see section 3.2.2) one gets $ik_m(C_0 \star U_{1mn})_0 + l_n(C_0 \star V_{1mn})_0 = 0$, and hence:

$$\frac{d\hat{h}_{mn}}{d\tau} = \omega_{mn}\hat{h}_{mn} \tag{23}$$

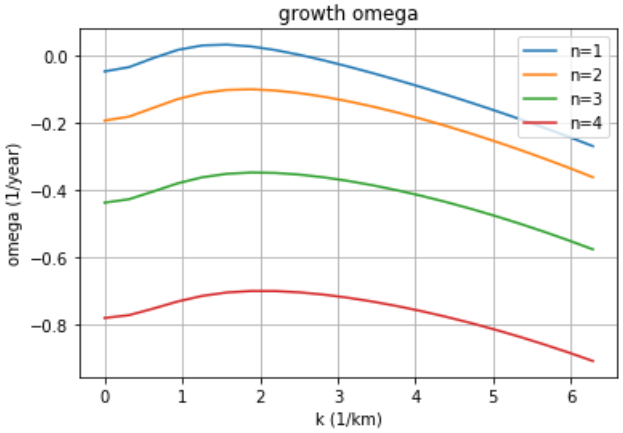

Figure 9: The ω-curves for the Exe estuary.

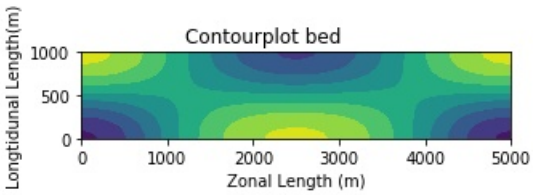

Figure 10: The associated bed pattern for the Exe estuary with the linear system: dominated by the $(1,1)$-mode. Troughs in blue and crests in yellow.

with

$$\omega_{mn} = \frac{1}{1-p}\Big(\frac{ik_mU}{2}(C_{1,m,n,1}+C_{1,m,n,-1}) + \mu(k_m^2+l_n^2)C_{1mn0} + \mu\frac{w_s}{\kappa_v}\beta_b C_{0,0}(k_m^2+l_n^2) + \hat{s}k_*\frac{4U^3}{3\pi}(k_m^2+l_n^2)\Big). \tag{24}$$

This explains the exponential behaviour of the amplitude: the ω-curves in figure 7 can be reproduced by only using expression (24).

4.2 Physical interpretation

More importantly, the exact expression in equation (24) helps with interpreting the physical concepts behind the sediment transport processes. The expression consists of four different terms. The initial $1/(1-p)$ is simply due to porosity of the sand. The four terms, which are described in the next two subsections, are plotted in figure 11 for the Western Scheldt.
A detailed description of the physics behind the unstable modes can be found in Schramkowski et al.(2002) and Hepkema et al.(2019).

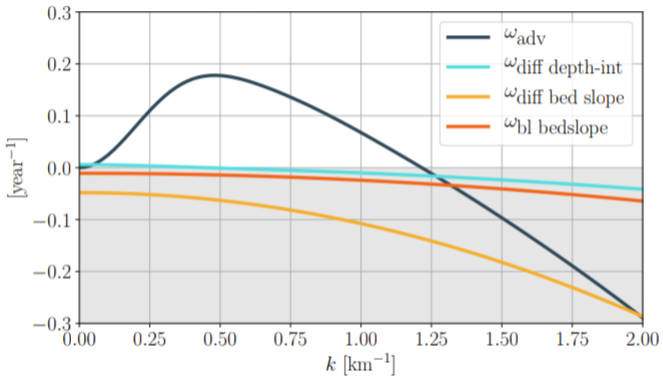

Figure 11: The four terms in expression (24): advection, depth integrated diffusion, bed slope diffusion and bed load transport due to slope plotted for Western Scheldt. Source: Hepkema et al.(2019)[5].

4.2.1 Advection

The first term is the advective term $\omega_{adv} = \frac{ik_m U}{2}(C_{1,m,n,1} + C_{1,m,n,-1})$: it is the result of advective sediment transport. It relates to the advective terms in the linear part of the bed-evolution equation in section 3.1.5: $C_0 \nabla \vec{u}_1 + u_0 \frac{\partial C_1}{\partial x}$. Sediment C_1 is transported by equilibrium current u_0, and equilibrium concentration C_0 is transported by current $\vec{u}_1$. However, as previously stated, due to C_0 only having constant on second temporal Fourier-coefficient, the latter transport becomes net zero over a tidal period, and so it disappears in expression (24). Therefore the only net advective transport in the linear system is the ebb and flood currents u_0 transporting sand C_1.
Analysis (see figure 11) shows that w_{adv} is the main driving force behind growing, unstable modes. Essentially in these modes advection causes crests to rise and troughs to deepen. The physical process behind this mechanism can be seen when plotting the residual current $\vec{u}_{res} =< \vec{u} >$: it shows the average current behaviour during a tidal cycle, see figure 12. Residual vorticity cells can be clearly seen. The cross-channel depth variations cause different frictional forces on the ebb and flood current (see red arrows in figure 13): crests causes an higher friction force, while the friction force is lower over troughs. This causes a lateral difference in velocity, which in turn generates a tidal vorticity (see the red circles). Now, this vorticity is subsequently transported by the ebb and flood currents (u_0). As a result, during ebb and flood there is a net influx of vorticity of the same sign into the regions between crests and troughs. All in all, residual vorticity builds up in these areas (black circles in the figure 13).
Then lastly remains to see why this vorticity build-up causes the growth of bars and deepening of troughs. Roughly speaking, the velocity in the vortex is high above the troughs, and here sand is 'picked up' due to erosion, while above the crests with low velocity erosion is low and here there will be a net deposition of sand. Since this effect will increase by a larger height difference, height differences amplify themselves, and thus one can intuitively expect exponential growth.
The main effect of the channel depth H can be seen by looking at the vorticity equation(see section 3.2.2):

$$i\sigma p E_{1mnp} + \nu(k_m^2 + l_n^2)E_{1mnp} + i\frac{Uk_m}{2}(E_{1,m,n,p-1} + E_{1,m,n,p+1}) + \frac{r}{H}E_{1mnp} = \frac{-Ur}{2H^2} l_n (H_{1,m,n,p-1} + H_{1,m,n,p+1}).$$

The first term is inertia, the second is dissipation of vorticity due to viscosity and the third is advection of vorticity. However, the most important are the fourth, which is dissipation of vorticity due to friction, and which goes like $\sim H^{-1}$, and the fifth, on the right-hand side, which is the creation of vorticity due to the friction-effects that were just described and which goes like $\sim H^{-2}$. So creation of vorticity decays faster with increasing H than the dissipation of vorticity: so an increase in H causes a decrease in the advection-effect, and so -as observed- an higher H will cause lower growth rates. Provided of course that other characteristics, like the channel width, are unchanged.

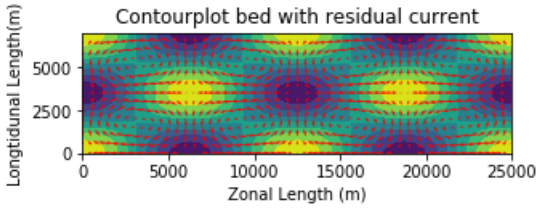

Figure 12: The bed pattern of the Western Scheldt (dominated by $(2, 2)$-mode) in the linear system with the residual current. Troughs in blue and crests in yellow.

4.2.2 Other processes

The second term in (24) is $\omega_{diffdepth-int.} = \mu(k_m^2 + l_n^2)C_{1mn0}$ the depth-integrated diffusion term. When at one location the depth-integrated concentration C is larger than a another, a diffusive transport occurs

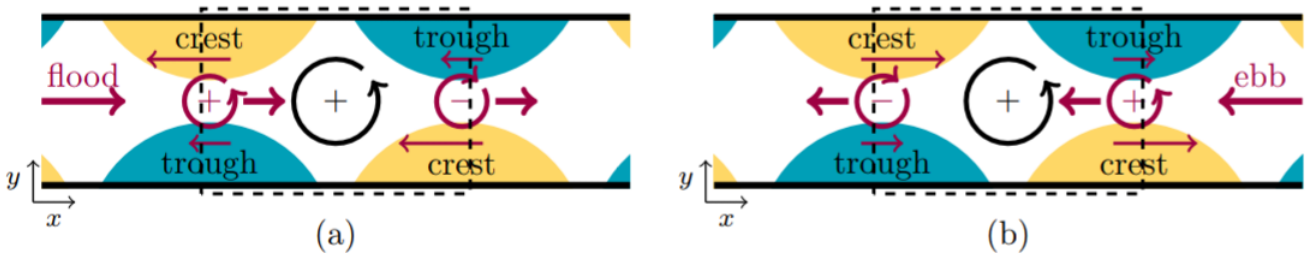

Figure 13: The generation of residual vorticity cells for bottom patterns with mode $n = 1$, although similar cells are also present in higher modes. The situation **(a)**During flood ($u_0 > 0$) and **(b)**During ebb ($u_0 < 0$). Friction forces (thin red arrows) is larger on crests and lower on troughs. This causes vorticity cells (red circles). Both during ebb and flood a net positive vorticity is transported into the dashed box. This results in the build-up of positive residual vorticity (black circle). Source: Hepkema et al.(2019)[5].

from high to low C. Generally $\omega_{diffdepth-int.}$ is close to zero.
Then the third term is $\omega_{diffbedslope} = \mu \frac{w_s}{\kappa_v} \beta_b C_{0,0} (k_m^2 + l_n^2)$ the diffusive bed-slope term. It relates to diffusive transport due to differences in bed height. If one has uniform depth-integrated concentration C on a sloping bottom, then the actual concentration of suspended sand is larger in shallower water columns than in deeper water columns. As a result, diffusive transport will occur from shallow to deep regions, although depth-integrated concentration is equal, see figure 14. Since sand is transported from shallow to deep: it dampens the bed amplitude. This effect increases with the slope of the bed, hence it increases with higher mode-numbers and will decrease the exponential growth rate of the height amplitude.
The last term is the bed slope term $\omega_{bottombedslope} = \hat{s} k_* \frac{4U^3}{3\pi} (k_m^2 + l_n^2)$. This relates to the bed load transport: sand is transported downward from crests to troughs. It has a damping effect and increases with height difference. Therefore it has a decreasing addition on the exponential growth rate, and the effect increases with higher wave modes. The importance of damping of the higher modes via bed load transport has been emphasized in Schramkowski et al.(2002): it prevents the higher modes causing an infinite 'braiding pattern'.

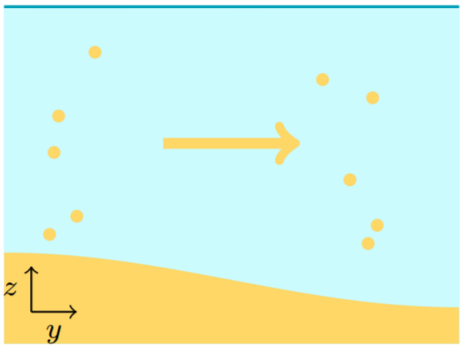

Figure 14: Given a uniform depth-integrated concentration C over a sloping bottom. On the left the water column is shallower than on the right, so the concentration of sand is larger on the left than on the right. Simply because the same amount of sand is present in a smaller water column. This results in diffusive transport of sand from left to right. Source: Hepkema et al.(2019)[5].

4.3 Summary

Firstly, the exponential growth of the amplitudes and the absence of interaction follows directly from the linear system. This system is valid as long as the disturbance h_1 is small, so that only first order ϵ terms are significant. The modes have different growth rates, some are positive, some negative. The dominant wave-mode has the largest growth rate and is the dominant pattern of the sandy bed. Its wave-numbers are not too high, since high wave numbers have a large damping effect due to bed load slope effects, neither too low, since advection is low at low wave numbers. This last effect is due to a lack of erosion and deposition at low wave numbers: the bed is namely near flat. Lastly, for increasing H or decreasing B less modes become unstable and the dominant wave-modes have lower numbers. This is mainly due to a large H causes more dissipation of vorticity, which causes a decrease in growth rates. A small B causes the same wave modes to have steeper slopes, and hence increases damping due to bed load, hence the dominant mode shifts to lower wave numbers.

5 Second-order results & discussion

When incorporating the second-order or even the third-order system into the calculation of the sediment transport, non-linear interactions become relevant. Looking at the equations in sections 3.2.3 and 3.2.4 one can see convolutions: this means that different (m, n)- modes interact with each other and can together amplify or dampen other modes. Due to this interaction modes that were stable in the linear system can suddenly be amplified, will the unstable modes in the linear system can now be dampened due to these non-linear interactions. These modes no longer grow exponentially. Hopefully, incorporating the non-linearity up to second- or even third-order will cause the modes to no longer grow above the water surface, and to form a finite-amplitude equilibrium in the estuary.

In figure 15 the amplitude evolution of the Western Scheldt is shown for interactions up to $\mathcal{O}(\epsilon^2)$, with random initial values for the amplitudes. This figure is representative for the results from the second-order system. From the linear results followed that $(2, 2)$ is the dominant mode for this channel, and indeed this is still the main mode. Initially the system exhibits linear behaviour: the dominant mode $(2, 2)$ grows exponentially, while the other modes are left behind. After some 45000 tidal cycles (60 years) the second-order behaviour can be seen: modes $(4, 4)$ and $(4, 0)$ rise fast. However, the second-order behaviour does not significantly influence dominant mode $(2, 2)$ and eventually the crests rise above the water surface: no equilibrium is reached. With this amplitude evolution an elongation of the troughs can be seen, see figures 16 and 17 for the bed patterns associated with figure 15.

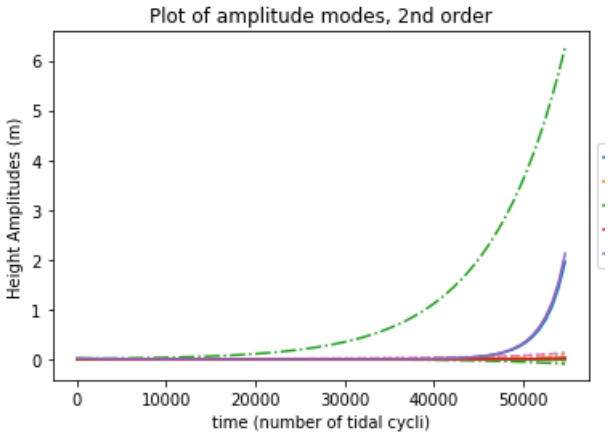

Figure 15: Amplitude $|\hat{h}_{mn}|$ evolution for second-order system, Western Scheldt. Modes $(2, 2)$(green), $(4, 4)$ (purple) and $(4, 0)$(blue). Used truncation parameters $M = 4$ and $N = 4$.

5.1 Interpretation

As stated before, initially the amplitudes behave linearly, since ϵ is still small. Once the bed has grown substantially, ϵ is no longer small, and second-order ($\mathcal{O}(\epsilon^2)$) become significant. Looking at the second-order equations (see section 3.2.3) and the second-order part of the bed evolution equation (section 3.2.5) one can see that the second-order amplitudes of current and concentration are linearly dependent on the convolutions of pairs of coefficients of first order variables $\vec{u}_1$, C_1, η_1 and h_1. Since these first three all dependent linearly on h_1: the second-order variables are quadratic in h_1, via the convolutions of pairs of $\hat{h}_{mn}$-amplitudes. Now, as explained before, the convolutions cause modes (a, b) and $(m-a, n \pm b)$ to form a contribution to the (m, n)-mode. So, heuristically, the differential equation for the bed evolution in the

second-order system:

$$\frac{d\hat{h}_{m,n}}{d\tau} = \omega_{m,n}\hat{h}_{m,n} + \epsilon \sum_{a=-M,b=-N}^{M,N} \left((\alpha_{m,n,a,b})\hat{h}_{a,b}\hat{h}_{m-a,n-b} + (\beta_{m,n,a,b})\hat{h}_{a,b}\hat{h}_{m-a,n+b}\right) \tag{25}$$

with coefficients α and $\beta[\mathrm{m}^{-1}\mathrm{s}^{-1}]$. Now, no significant damping of modes due to second-order effects has been observed, so it is assumed that the coefficients α_{mn} and β_{mn} for second-order interactions are in general non-negative.
This specific case in figure 15 can be clarified by equation (25). Initially in the linear regime the dominant mode $(2, 2)$ dominates the channel, and all other amplitudes seem insignificant. Once second-order interactions become relevant, interactions between pairs of amplitude occur. The only significant interactions is of mode $(2, 2)$ with itself: all other amplitudes are small compared to $(2, 2)$ and hence have no powerful contributions. The interaction of $(2, 2)$ with itself affects the evolution of modes $(4, 4)$ and $(4, 0)$ (see equation (25)). Hence, the modes $(4, 4)$ and $(4, 0)$ rise (via the second-order interactions only, since $\omega_{4,4} < 0$ and $\omega_{4,0} < 0$). This is the elongation of the troughs. There is no new mode due to interactions with then now significant modes $(4, 4)$ and $(4, 0)$: the truncation of spatial Fourier-analysis stops at $M = 4$, $N = 4$, and the crests have already reached the surface.
There are no new physical processes occurring at second order: the same processes in the linear regime (advection, diffusion and bed slope) occur in the second-order system with magnitude $\mathcal{O}(\epsilon^2)$. The main driver of the growing modes, $(2, 2)$, $(4, 0)$ and $(4, 4)$ will be advection, just as in the linear case. In figure 18 the bed with elongation is plotted with the residual velocity. The vortexes associated with $(2, 2)$-mode are present and cause advection, just as in the linear case. However, due to the extra $\nabla(\vec{u}_1 C1)$ in the advection in equation (18) there is a convolution in the advection terms. Hereby the vortexes caused by the $(2, 2)$-mode generate advective sediment transport to the $(4, 4)$ and $(4, 0)$-mode.
The elongation of the troughs is due to the geometry of the channel. The along-channel dominant mode $m = 2$ interacts with itself and doubles to $m = 4$: it is free to do so since there are no closed boundaries at the channel's end. However, for the cross-channel mode: $n = 2$ interacts with itself and creates $n = 4$, but also $n = 0$. This last mode is also created due to the closed boundaries at the channel's sides: the (co)sines needed to fulfill the cross-channel boundary conditions cause this extra mode. Next to $(4, 4)$ also $(4, 0)$ is created: this is the elongation.

5.2 Summary

In the second-order system the dominant mode from the linear regime continues to determine the pattern of the bed. Eventually the second-order results start to show with mainly the dominant mode interacting with itself. This causes elongation of the troughs, which is the along-channel direction due to the geometry of the channel.
The elongation was also found by Olabarrieta et al.(2017) in the tidally dominated (parts of the) estuaries. Also, in the equilibria found by Schramkowski et al.(2004) elongation of the troughs was observed.
Unfortunately, the second-order interactions are too slow to dampen the dominant mode. So can $(2, 2)$ 'excite' mode $(4, 4)$, but for -for example- mode $(4, 4)$ to interact with $(-2, -2)$ to in turn dampen $(2, 2)$ is not enough time: usually the crests have already surfaced.
It could be expected that no equilibrium would occur. Blondeaux & Vittori (2008)[1] used a second-order system to analyze a three-dimensional model for tidal sand waves in open seas, and also in their case the modes eventually grew out of the water. Furthermore, their paper also found that the non-linearity of second-order interactions caused some elongation in their bathymetric patterns.

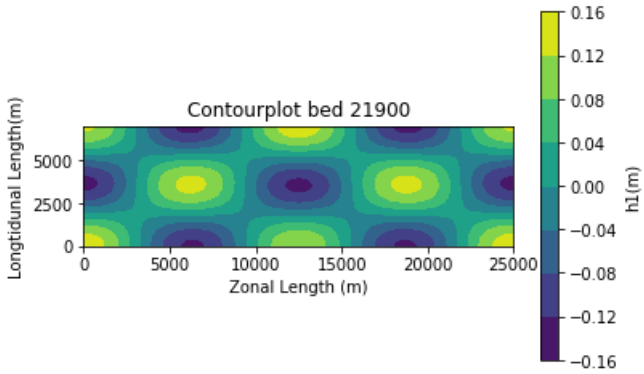

Figure 16: Western Scheldt is still in linear regime after 30 years (21900 tidal cycles): pattern is in dominant mode $(2, 2)$.

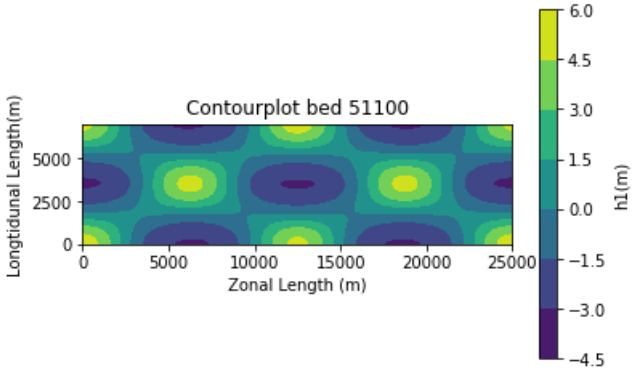

Figure 17: After 70 years (51100 tidal cycles): the second-order effects are visible and the troughs in the Western Scheldt are elongated.

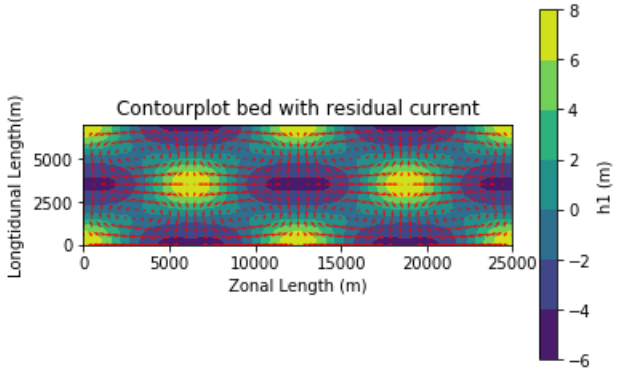

Figure 18: Western Scheldt in second-order system: elongated channels with residual velocity.

6 Third-order results & discussion

In figure 19 the amplitude evolution of the Western Scheldt is shown for interactions up to $\mathcal{O}(\epsilon^3)$, with the same initial values for the amplitudes as in figure 15. This figure is representative for the results from the third-order system. Again, initially the system behaves linearly with dominant mode $(2,2)$. After roughly 40000 tidal cycles (60 years), like before, the second-order effect is shown with the rise of the $(4,0)$-mode. Also the $(4,4)$-mode rises,, but is not a prominent. The important feature of the third-order system is visible after 70000 tidal cycles (100 years): the dominant $(2,2)$-mode damps! At the end, the $(4,0)$-mode keeps growing and causes the crests to surface. Associated with the final dominance of the $(4,0)$-mode is the crests making cross-channel contact with each other. The bed patterns associated with figure 19 can be seen in figures 20 and 21.

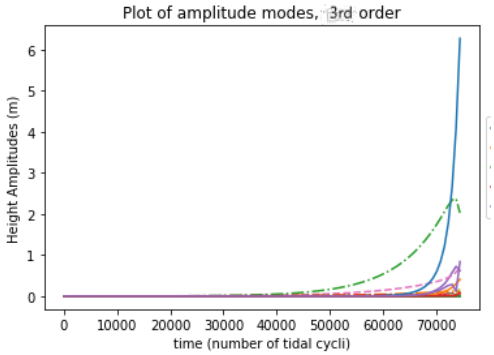

Figure 19: Amplitude evolution for third-order system, Western Scheldt. Modes $(2,2)$ (green) and $(4,0)$ (blue). Truncation with $M = N = 4$.

6.1 Interpretation

The rise of the $(4,0)$-mode is caused by the second-order interactions, as explained before. Now due to the damping of the $(2,2)$-mode, the $(4,0)$-mode fully determines the bed topography. Also due to this damping the shoals breach the surface later, and gives the $(4,0)$ more time to grow. The pattern associated has not only elongated channels, but also the across-channel crests.
The most important characteristic of the third-order system is the damping of the dominant mode. This can be clarified by analyzing the third-order system in section 3.2.4 and the third-order part of the bed evolution equation in section 3.2.5. From the third-order system equations follows that the third-order variables $(\vec{u}_3, C_3, \eta_3)$ are linearly dependent on the convolution of three h_1-coefficients. This follows from the fact that the first-order are linearly in h_1 and the second-order variables are quadratic in h_1. Now, three different height amplitudes can, via two convolutions, influence the evolution of another amplitude. Heuristically, one could expect the differential equation in the third-order system to be something similar to:

$$\begin{aligned}\frac{d\hat{h}_{m,n}}{d\tau} = \omega_{m,n}\hat{h}_{m,n} + \epsilon \sum_{a=-M,b=-N}^{M,N} \left((\alpha_{m,n,a,b})\hat{h}_{a,b}\hat{h}_{m-a,n-b} + (\beta_{m,n,a,b})\hat{h}_{a,b}\hat{h}_{m-a,n+b}\right) \\ +\epsilon^2 \sum_{\substack{i,j,k=-M \\ i+j+k=m}}^{i,j,k=M} \sum_{\substack{a,b,c=-N \\ a\pm b\pm c=n}}^{a,b,c=N} \delta_{\substack{ijk \\ abc}} \hat{h}_{i,a}\hat{h}_{j,b}\hat{h}_{k,c}\end{aligned} \tag{26}$$

where δ $[\mathrm{m}^{-2}\mathrm{s}^{-1}]$ is some coefficient.
The relevant implication of equation (26) is that the dominant wave mode can now directly affect itself

via the third-order interaction. As an example is again referred to the situation in figure 19. The largest wave mode is $(2,2)$ and -until right before the end- it is also the only significant one. Now $(2,2)$ cannot directly affect itself via the second-order interaction: it can only do so directly to modes $(4,0)$ and $(4,4)$. However, via the third-order it is possible:

$$\begin{aligned}\frac{d\hat{h}_{2,2}}{d\tau} &= \omega_{2,2}\hat{h}_{2,2} + \epsilon^2\delta\hat{h}_{2,2}\hat{h}_{2,2}\hat{h}^*_{2,2} \\ &= \omega_{2,2}\hat{h}_{2,2} + \epsilon^2\delta\hat{h}_{2,2}|\hat{h}_{2,2}|^2.\end{aligned}$$

Note that the complex conjugate is $\hat{h}^*_{2,2} = \hat{h}_{-2,2}$, so that the conditions in equation (26) are fulfilled. Indeed, $\hat{h}_{2,2}$ not only affects its own evolution via the linear system, which causes exponential growth with $\omega_{2,2} > 0$, but via the third-order interactions is direct feedback also possible.
Why this evolution equation causes the dominant mode to decay, can be seen by looking at the famous *Stuart-Landau* equation:

$$\frac{dA}{dt} = \omega A - \phi A|A|^2 \tag{27}$$

where $A \in \mathbb{C}$, and ω and ϕ are complex coefficients. This equation generally occurs in weakly non-linear systems, such as this system where the most dominant mode is still determined by the initial linear interactions. The amplitude $|A|$ converges eventually following equation (27) to $(\frac{2\Re(\omega)}{\Re(\phi)})^{\frac{1}{2}}$ for $t \longrightarrow \infty$. This equation occurs in a lot of different non-linear systems, and more can be found in *Chemical oscillations, waves, and turbulence*[8].
Following the similarity between the *Stuart-Landau* equation and the $\hat{h}_{2,2}$-equation it can be expected that the dominant $(2,2)$ decays to a stable level as long as $\epsilon^2\delta^2$ has a real part and $(\frac{2\omega_{2,2}}{\epsilon^2\Re(\delta)})^{\frac{1}{2}} \ll H$. This seems to be indeed the case in figure 19. Also in other third-order simulations decays the dominant mode eventually, so the *Stuart-Landau* equation seems to be also present in these cases.
To verify that the dominant mode follows the *Stuart-Landau* equation a simulation is done for the Netarts-estuary where the dominant mode is $(1,1)$. All other modes are only subjected to linear equations, so $\frac{d\hat{h}_{mn}}{d\tau} = \omega_{mn}\hat{h}_{mn}$ for $|m| > 1 \vee |n| > 1$, while $(1,1), (1,0), (0,1)$ are the only modes subjected to third-order interactions. So all other modes are either small or decay to zero, and $(1,1)$ is 'free' to follow *Stuart-Landau* without interference from rising higher modes like $(4,0)$. The result is shown in figure 22: indeed $(1,1)$ decays to a stable level. It shows that a mode on its own can stabilize itself.
In the third-order system there are no new physical processes that are responsible for the decay. The decay is not due to a new sand transport to other modes but is the purely mathematical consequence of adding higher order interactions. Hence, the decay can be viewed as a correction of the unrealistic unrestricted exponential growth of the linear results: a mode eventually 'corrects' itself.

6.2 Summary

In the third-order system the dominant mode from the linear regime eventually decays. The decay can be explained through the *Stuart-Landau* equation. The occurrence of *Stuart-Landau* was in the third-order evolution equation was expected. In the hope of finding the convergences of the solutions of the *Stuart-Landau*, and hence some equilibrium in the estuary, the variables in (9) are expanded till third-order $\mathcal{O}(\epsilon^3)$.
The bed topography is mainly determined by modes that are excited by the dominant mode via second-order interactions. These cause elongation of the channels and widening of the crests. This is also observed in the equilibria of Schramkowski et al.(2004): "the shoals appear to be connected by shallow 'bridges' that divide the bathymetry into deep but separated 'pools'".
However, the system does not reach an equilibrium since the higher modes breach the surface. These modes apparently do not damp in the same way as and as fast as the dominant mode.

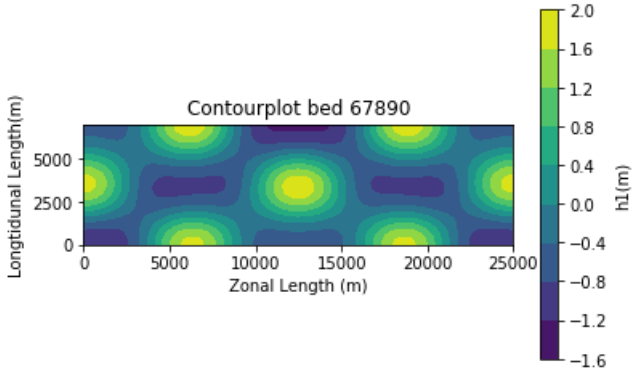

Figure 20: Western Scheldt is still in second-order regime
after 90 years (67890 tidal cycles): pattern has elongated channels.

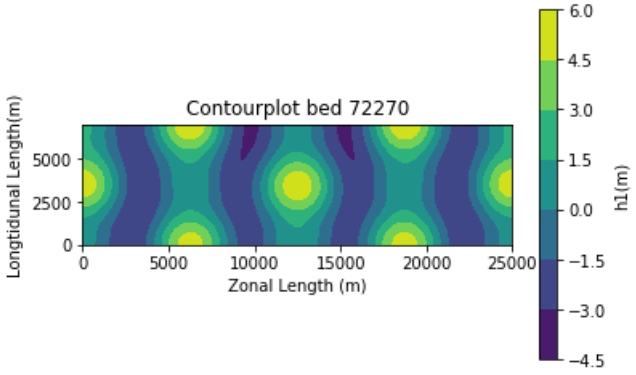

Figure 21: After 100 years (72270 tidal cycles): the third-order effects are quickly visible. The damping of $(2, 2)$ and rise of $(4, 0)$ causes the crest to touch each other across the Western Scheldt.

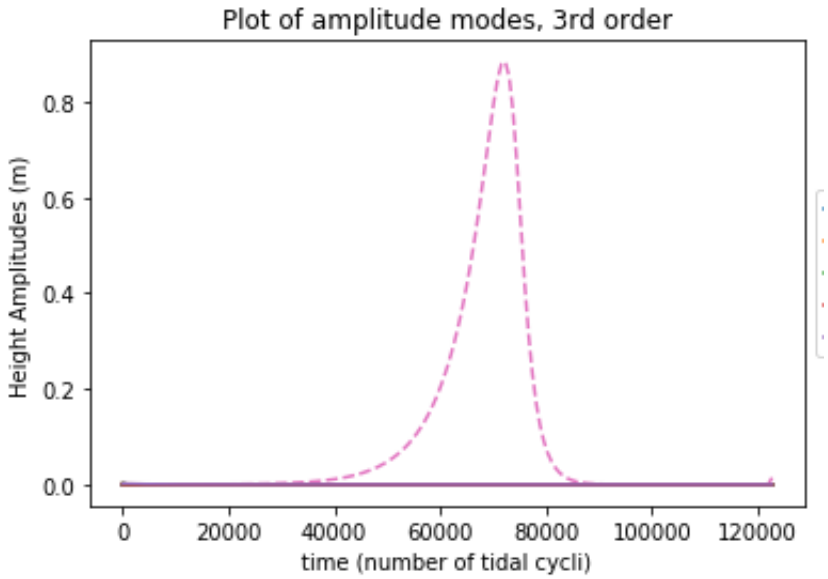

Figure 22: Amplitude evolution for dominant mode subjected solely to third-order system, Netarts Bay. Mode $(1, 1)$ (orange) with truncation $M = N = 4$.

7 General Discussion

Looking at the second- and third-order results there are no equilibria reached. The root causes for this are inherent to the methods used.

7.1 Truncation of spatial modes

The simulations in the second- and third-order regime all end rather abruptly due to the rising higher modes. These modes are excited by the original dominant mode: sand eroded from the dominant mode is disposed in the pattern of the higher modes. Potential energy from small modes is cascaded towards the higher modes. The key problem is that these higher modes cannot lose this energy to other modes via the second- and third-order interactions. Due to the truncation the highest modes are limited to M, N, and, as seen in figures 15 and 19, these highest possible modes keep on rising.
Of course a possible solution is to include more modes. This way the energy can cascade further down, and spread via the second- and third-order interactions over more modes. Simulations have been done for as high as $M = N = 10$. However, even here, be it after some centuries, the highest modes eventually rise and the crests breach the water surface. The hope was that the energy would be spread over a lot of high modes, and that damping due to bed slope (which increases quadraticly with mode numbers) would be enough to dampen these modes. It seems that the high spatial modes in the estuaries are not as effective in dissipating energy as the high spatial modes in the shallow shelf seas of Van Veelen et al.(2018).
This difference is due to the geometry of the estuary. Look for example at figure 23: the rising modes which cause the surface breach are $(6, 3)$ and $(6, 4)$. The energy cascade in the longitudinal direction seems very effective: mode $m = 6$ is quickly reached. However, the cascade in the cross-channel direction is slower: rising modes at the end include $n = 4$ and $n = 3$. In the longitudinal direction the channel is infinite and acts similar to the open seas of Van Veelen et al.(2018): modes m_1 and m_2 form $m_1 + m_2$. But in the cross-channel direction there are closed boundaries. This causes modes n_1 and n_2 not only to form higher mode $n_1 + n_2$ but also to contribute downward to mode $n_1 - n_2$ (see section 3.2.1). Therefore the energy cascade in the lateral direction is not as fast as in the longitudinal direction. Hence, the energy is already 'stuck' in the end at $m = M$, while the lateral modes n are still relatively small. This makes the dissipation of energy via damping less effective compared to a completely open sea.
As a last resort one could dramatically increase M, N, hoping that the longer cascade in the along-channel direction will buy enough time for the energy to be distributed and dissipate in the lateral direction. However, then a practical problem needs to be faced. The convolution functions consist of number of terms of magnitude $\mathcal{O}((2M + 1)^2(2N + 1)^2(2P + 1)^2)$. Where a simulation with $M = N = 4$ and $P = 2$ costs a couple of hours of computer-time, one with $M = N = 8$ and $P = 2$ costs nearly two days! So M, N have to be reasonable in order to keep the CPU-time manageable. Another way to approach this 'ineffective energy cascade-problem' could be to initially start of with low potential energy. Starting off with only one unstable mode in a deep, narrow channel. This is the near-critical condition: the channel is just on the verge of being a completely flat bed, see figures 24 and 25 . That especially this case could result in an equilibrium, based on the findings of Schramkowski et al.(2004). But figure 25 shows that this just delays the inevitable rise of the higher modes.

7.2 Higher order interactions

Instead of adding more spatial modes in attempt to deal with the problem of fast rising higher modes, one could also expand the current and concentration variables in higher powers of ϵ. Adding third-order interactions gave a whole new range of possibilities for some amplitudes to directly affect other amplitudes, one of these possibilities was $(2, 2)$ to directly weaken itself. Maybe adding fourth- or even fifth-order

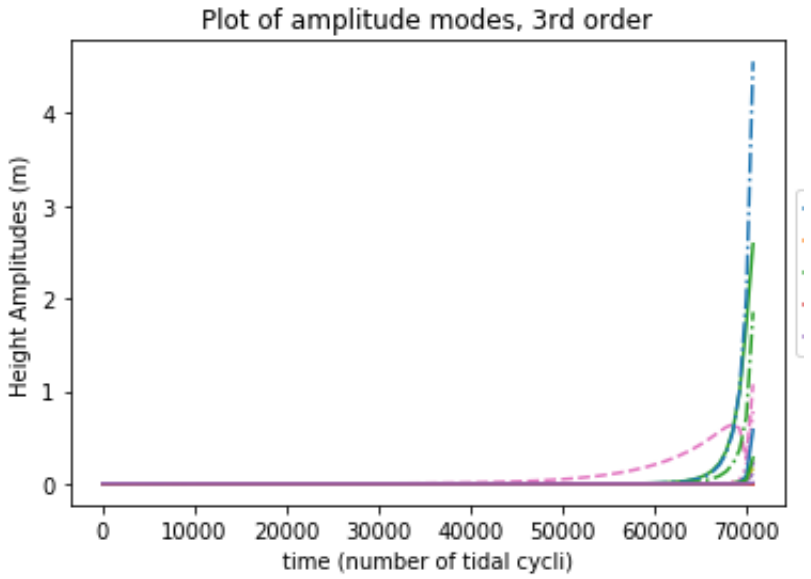

Figure 23: Amplitude evolution for third-order system, Netarts Bay. Mode $(1,1)$ (pinks) eventually decays, with fast rising modes $(6,3)$ (green solid), $(6,4)$ (blue) and $(6,6)$ (green dashed) with truncation $M = N = 6$.

interactions gives the possibility for the higher spatial modes to have other large high modes to directly affect via the extended bed evolution equation. This could in turn solve the problem of the ineffective damping of these high modes. For example, Van Veelen et al.(2018) used interactions up to tenth-order of ϵ.
However, adding higher orders into the equation would cost a lot more CPU-time to calculate the final sediment transport. Also, adding higher orders would defeat the original purpose of the asymptotic analysis of this model: using relatively simple mathematical methods to eventually get an equilibrium in the estuary. Making the asymptotic analysis more complex prevents the goal of attaining some fundamental physical insight in the processes involved in an equilibrium.

7.3 Surface Breaching

A more fundamental problem may be with the used model. In the model crest may not rise above the surface. If $h > H$ then the friction force $\vec{F}_r$ would pass through a singularity and suddenly become positive and directed along the current. But, looking at figures 1 and 2 one could ask if it is realistic to demand that the tidal bars have to be subsurface. In Van der Wegen & Roelvink(2008) a model is used where drying and flooding is incorporated: if area cells in the model fall dry, they are removed from the hydrodynamic calculations and if they get wet again, they are included into the hydrodynamica.
However, this makes the model more complicated, which defeats the purpose of using simplified systems: to get insight in the physical processes. Moreover, Schramkowski et al.(2004) shows that the subsurface model is sufficient for creating equilibria. Lastly, allowing crests to rise above the surface would lead to $\epsilon \approx 1$, which makes the asymptotic expansion invalid.

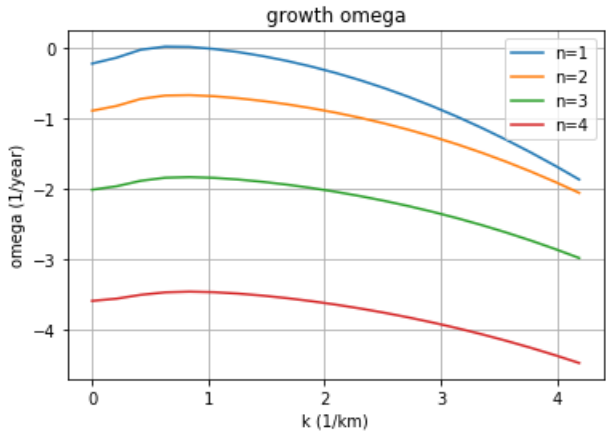

Figure 24: The ω-curves for near-critical situation, with B=1km, U=1m/s and H=10m.

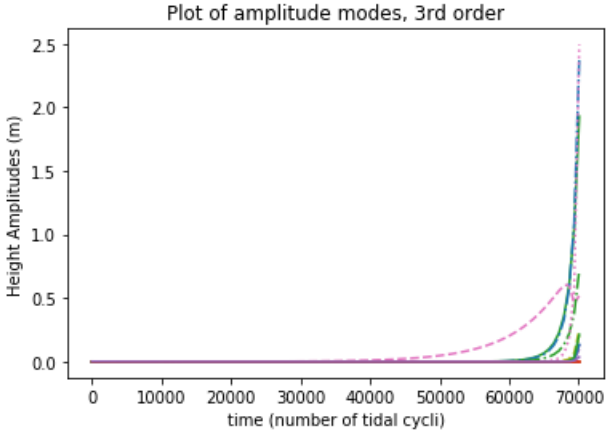

Figure 25: The amplitude evolution for the near-critical situation with third-order interaction: dominant mode $(1,1)$ (pink dashed) initially, then $(2,2)$ (green dashed), $(3,1)$(pink speckled) and $(4,0)$ (blue) rise at the end. Section length $L = 8$km used.

8 Summary & Conclusion

Asymptotic analysis is applied to an idealized model of tidally dominated estuaries in order to find out what bathymetric features could be reproduced, with emphasis on the creation of a finite-amplitude equilibrium. The idea was inspired by Van Veelen et al.(2018) who applied the same methods to analyze tidal formations in open seas.

The linear results were a near-exact reproduction of Hepkema et al.(2019). The linear results clarified the main patterns observed in estuary. The increased tidal bar length with wider channels, and the stabilizing effect of depth can be clarified with the first-order equations. Moreover, the linearized system reproduced the instability of seemingly flat bed, as found by Seminara & Tubino (2001).

The second- and third-order results showed some expected features. The elongation of troughs and cross-channel shallow bridges of sand were observed, which were direct consequences of added interaction terms between spatial modes. These features were also observed in the equilibria from Schramkowski et al.(2004).

However, the finite-amplitude equilibria from Schramkowski et al.(2004) could not be reproduced. Even when using near-critical initial conditions the higher spatial modes still breached the surface. These high modes were not damped fast enough. The root causes were inherent to the model and method. That the energy dissipation in the estuary was not as fast as in Van Veelen et al.(2018) was mainly due to geometry: a semi-closed estuary did not allow a fast energy cascade to and eventual damping of the high modes compared to an open sea. Moreover, the number of modes in the model had to be limited to keep CPU-time manageable. Therefore, simply using a lot of modes in order to have more dissipation for a finite-amplitude equilibrium was not an option.

All in all, asymptotic analysis could not create the desired finite-amplitude equilibrium, which is the most important consequence of the non-linear dynamics. Therefore is asymptotic analysis not suitable to clarify the non-linear effects in estuaries.

References

[1] P. Blondeaux and G Vittori. *Three-dimensional tidal sand waves.* Journal Fluid Mechanics, 2009.

[2] Cushman, Roisin, and Becker. *Geophysical Fluid Dynamics.* Elsevier Science Publishing, 2011.

[3] J. Hazewinkel. *Lorentz linearization and its application in the study of the closure of the Zuiderzee.* Physics of Coasts, 2004.

[4] T.M. Hepkema. *Asymptotic analysis of nonlinear tides in Wadden systems - the role of momentum sinks.* University Utrecht, 2016.

[5] T.M. Hepkema, H.E. de Swart, and H.M Schuttelaars. *The sensitivity of tidal bar wavelength to channel width.* Journal of Geophysical Research: Earth Surface, 2019.

[6] M.H. Holmes. *Introduction to Perturbation Methods.* Springer, 2012.

[7] M.C.J.L. Jeuken. *On the Morphologic Behaviour of Tidal Channels in the Westerschelde Estuary.* Netherlands Geographical Studies, 2000.

[8] Y. Kuramoto. *Chemical oscillations, waves, and turbulence.* Springer, 2012.

[9] J.R.F.W. Leuven, M.G. Kleinhans, S.A.H. Weisscher, and M. van der Vegt. *Tidal sand bar dimensions and shapes in estuaries.* Elsevier Earth-Science Reviews, 2016.

[10] H.A. Lorentz. *Het in rekening brengen van den weerstand bij schommelende vloeistofbewegingen.* De Ingenieur, 1922.

[11] M. Olabarrieta, W. Rockwell Geyer, G. Coco, C.T. Friedrichs, and Z. Cao. *Effects of Density-Driven Flows on the Long-Term Morphodynamic Evolution of Funnel-Shaped Estuaries.* Journal of Geophysical Research: Earth Surface, 2017.

[12] G.P. Schramkowski, H.M. Schuttelaars, and H.E. de Swart. *The effect of geometry and bottom friction on local bed forms in a tidal embayment.* Continental Shelf Research, 2002.

[13] G.P. Schramkowski, H.M. Schuttelaars, and H.E. de Swart. *Non-linear channel-shoal dynamics in long tidal embayments.* Ocean Dynamics, 2004.

[14] G. Seminara and M. Tubino. *Sand bars in tidal channels.* Journal Fluid Mechanics, 2001.

[15] R. Soulsby. *Dynamics of Marine Sands.* Thomas Telford Publications, 1997.

[16] M. van der Wegen and H.M. Schuttelaars. *Long-term morphodynamic evolution of a tidal embayment using a two-dimensional, process based model.* Journal of Geophysical Research, 2008.

[17] T.J. van Veelen, P.C. Roos, and S.J.M.H. Hulscher. *Process-based modelling of bank-breaking mechanisms of tidal sandbanks.* Continental Shelf Research, 2018.